WAKE BOUNDARIES FOR OBJECTS PLACED IN OPEN CHANNELS

A Thesis

Presented in Partial Fulfillment of the Requirement for the

Degree of Master of Science

Major in Civil Engineering

in the

University of Idaho Graduate School

by

Liou, Chyr Pyng

June, 1972

AUTHORIZATION TO PROCEED WITH THE FINAL DRAFT:

This thesis of Liou, Chyr Pyng for the Master of Science degree with major in Civil Engineering and titled "Wake Boundaries for Objects Placed in Open Channels" was reviewed in rough draft form by each Committee member as indicated by the signatures and dates given below and permission was granted to prepare the final copy incorporating suggestions of the Committee; permission was also given to schedule the final examination upon submission of two final copies to the Graduate School Office:

Major Professor _____ Date June 8, 1972

Committee Members _____ Date June 20, 1972

_____ Date June 26, 1972

_____ Date June 27, 1972

REVIEW OF FINAL DRAFT:

Department Head _____ Date July 7, 1972

FINAL EXAMINATION: By Majority vote of the candidate's Committee at the final examination held on date of July 19, 1972. Committee approval and acceptance was granted.

Major Professor _____ Date July 19, 1972

GRADUATE COUNCIL FINAL APPROVAL AND ACCEPTANCE:

Graduate School Dean _____ Date 7-21-72

ACKNOWLEDGEMENTS

The writer would like to express his gratitude to his major professor Dr. F. J. Watts and to Dr. G. L. Bloomsburg of the Engineering Science Department, Dr. R. H. Goetschel of the Mathematics Department and Professor C. C. Warnick of the Civil Engineering Department for their guidance throughout this study. The writer is particularly indebted to Dr. Goetschel for his encouragement and suggestions.

The writer would like to thank Mr. H. M. Gibson and Mr. C. W. Clark who helped to construct experimental facilities.

The writer's graduate studies and research were financed by the Water Resources Research Institute of the University of Idaho; this assistance was deeply appreciated.

TABLE OF CONTENTS

LIST OF FIGURES

FIGURE Page

FIGURE Page

LIST OF TABLES

ABSTRACT

A new hodograph for the wake boundary behind a flat plate placed normal to the flow was developed and verified with experimental results. In this mathematical treatise velocities along the shear layer can vary. The classical Kirchhoff's solution is a special case of this model.

A comparison of the sizes of wakes produced by a flat plate, a 90-degree wedge, and a circular cylinder were made. The effect of the depth of water relative to the width of the obstacle, on the wake size was investigated. The shape of wakes produced by an embedded sphere with different degrees of submergence was also studied. All experimental work was done in a horizontal straight open channel using water as the experimental fluid.

CHAPTER 1

INTRODUCTION

Steady two-dimensional flow past bluff bodies at large Reynolds number is one of the oldest unsolved problems in hydrodynamics. The flow is bounded partly by rigid walls and partly by "free" streamlines of unknown shape and location. The region enclosed by the free streamline is defined as the wake. The pressure distribution along the "free" streamline is generally unknown. Considerable experimental and theoretical work to define the "free" streamlines encompassing the wake has been accomplished.

The fundamental work for solution of this problem was done by Helmholtz and Kirchhoff about a century ago. In their studies, the pressure on the streamline defining the wake was assumed to be constant and was equal to that at infinity. This streamline with an assumed constant pressure was then called "free". The applications of their theory to the cases of liquid flow of finite lateral extent surrounded by gas gave excellent results. This is because any motion which developed in the gas has a negligible effect on the liquid flow and therefore, the constant pressure assumption was realistic. As an example, the theoretical values of the contraction coefficient of a two-dimensional jet issuing through

a slot in a plane wall of a large vessel(10)* or flow under a sluice gate (9) are very close to the experimental result.

The free streamline theory, however, fails to predict the wake boundary when the fluids inside and outside the wake are of the same density. The reason for this failure is that although the velocity in the wake region close to the obstacle is generally smaller than that outside the wake, it is an over simplification to assume pressure near the obstacle is constant and is equal to the pressure at infinity.

In order to find a more realistic solution for the wake boundary, an understanding of the wake flow is necessary. Some basic concepts concerning the location of the wake boundary are discussed in Chapter 2. The wake flow phenomenon itself and free-streamline theory are described in Chapter 3 and in Chapter 4 a more realistic solution for the wake boundary of a flat plate placed normal to the flow is developed. The effect of gravity has been neglected in the mathematical model.

Wake boundaries were located for different obstacles in a straight open channel by using yaw and pitch probes. The apparatus used and the procedures employed are described in Chapter 5. Chapter 6 includes results and discussion and suggests additional studies which would advance the knowledge of wake flow. Chapter 7 is a summary stating what has been done and what has been found in this study.

---

*The numbers in parentheses refer to the references listed at the end of the paper.

CHAPTER 2

BASIC CONCEPTS

Separation Surface and Wake

Physically, the effect of viscosity in fluid flow is generally confined to the boundary layer next to the obstacle. In this layer, there is a rapid increase in velocity in the direction normal to the surface of the obstacle. If the obstacle is blunt, the attachment of the boundary layer over the whole surface of the body is impossible because of retardation of the external stream over the rear portion of the obstacle and hence, this condition results in an unsteady boundary layer (13).

The layer of fluid with rotation as described above is called the separation layer. If the velocity gradient over the layer is large enough, or the layer is thin enough, this layer can be approximated by a surface called the surface of velocity discontinuity or separation surface. In two-dimensional flow it reduces to a separation line. The shear layer and its approximation are shown in Figure 1. The region of non-zero vorticity behind the obstacle bounded by the body and separation lines is the wake as shown in Figure 2.

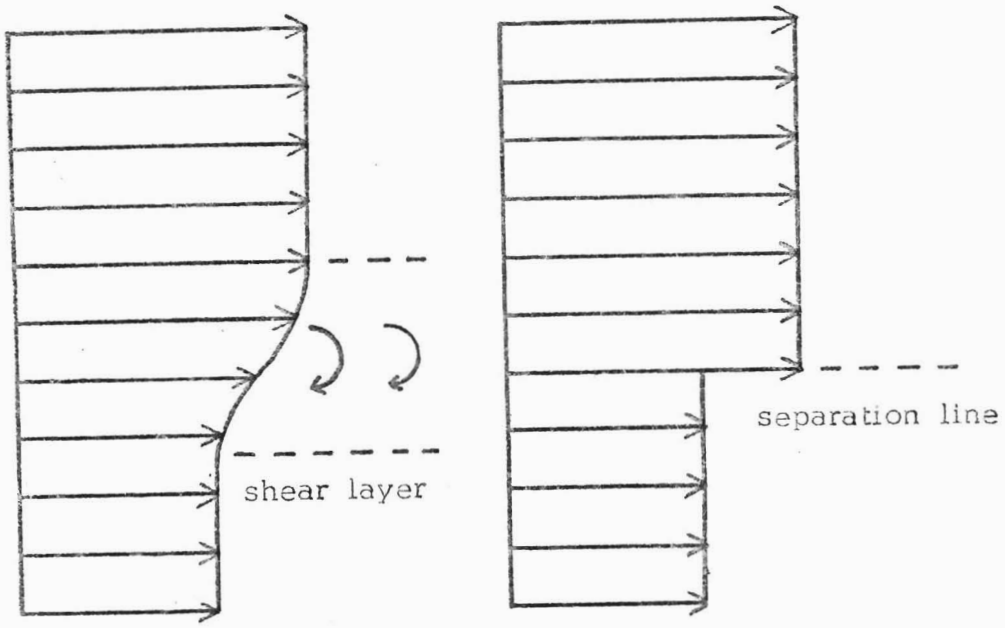

Figure 1. The shear layer and its approximation.

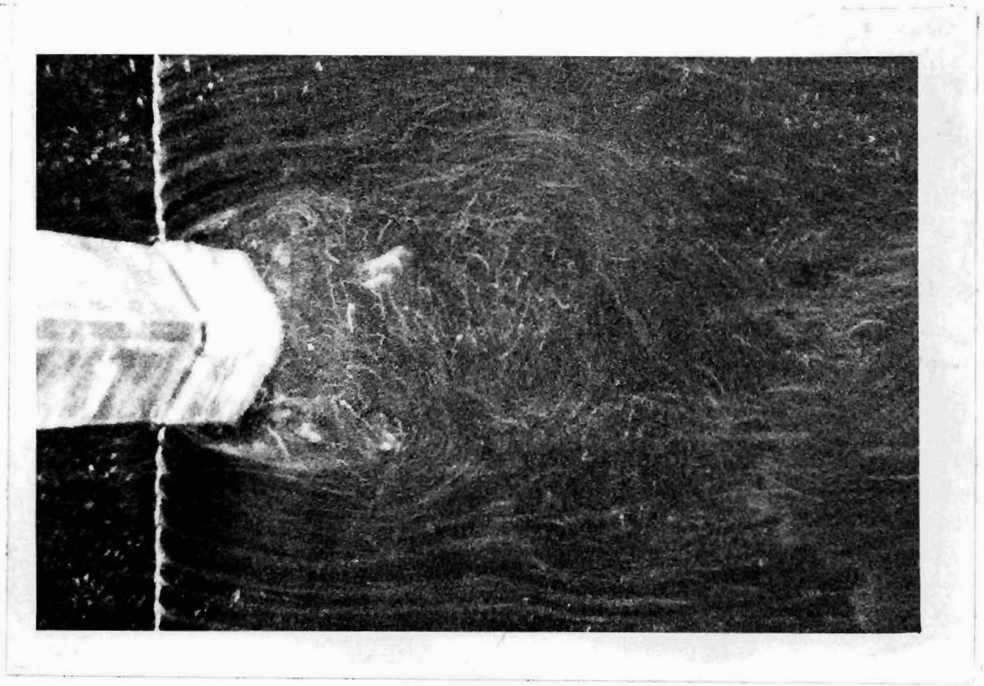

Figure 2. Shear layer and wake.

Nature of the Potential Flow and the Separation Line

Because of the converging boundary, the flow outside the wake immediately downstream from the obstacle is steady while the flow at a certain distance downstream is unsteady. When the Reynolds number, defined as $\frac{Ul}{\nu}$, is high, the flow can be treated as steady and consists of an extensive region of effectively non-viscous flow separated from the wake by the separation lines. The solution to this problem can not be accomplished unless certain assumptions are made about the pressure distribution along the separation line. For the case of steady flow, the pressure is related directly to velocities along the separation line through the Bernoulli equation. The position of the separation line which is a part of the flow boundary is not known a priori. Therefore, an assumption about the flow boundary has to be made before a solution can be attempted.

One basic nature of this type of flow is that maximum velocity occurs on the separation line (2). The immediate consequence is that the separation line must be convex as is readily shown using potential flow theory (17). In Figure 3 the pressure gradient along the normal to the separation line drawn into the flow is positive. Therefore, the acceleration of a fluid particle on the separation line is directed into the wake. If the flow is steady, the path of the particle is the separation line and it has to be convex.

The maximum velocity at the separation line will be used as the criterion to locate the wake boundary experimentally.

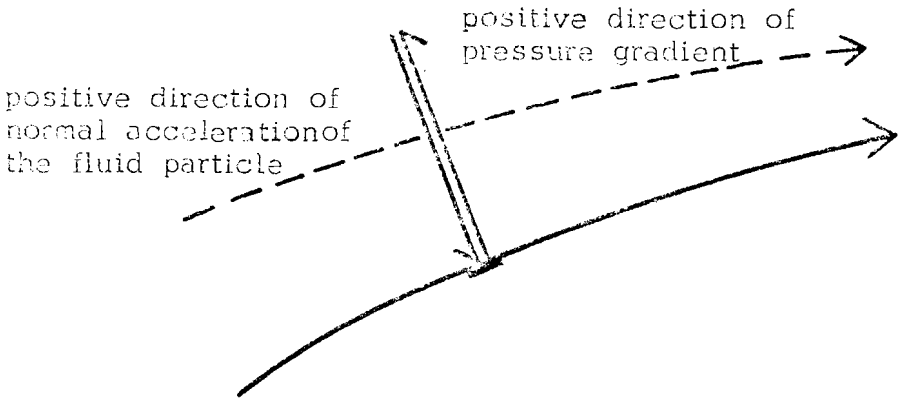

Figure 3. The effect of pressure distribution along free streamline.

The significance of the assumption concerning pressure distribution along the separation line is also shown in Figure 3. The variation of pressure acting on the fluid particle as it moves downstream will change its course; the shape and location of the wake boundary will change accordingly.

CHAPTER 3

LITERATURE REVIEW

Although wake flow itself is not the main object of this study, it is necessary to have a general understanding of the flow inside the wake and inside the shear layer so that reasonable assumptions can be made before solving the problem. The first part of this chapter is a description of the phenomena of the wake flow. The second half is a brief review of the free streamline theory and its variations.

Two-Dimensional Wake Flow Behind a Cylindrical Body

At very low Reynolds numbers, $R<1$, inertia terms in the equation of motion are negligible and the flow field can be approximated by Oseen's solution (5). A wake does not exist in the calculated streamline pattern.

Within the intermediate region, $1<R<100$, both inertia force and viscous force are of equal importance and neither can be neglected. Hence, it is difficult to solve the equation of motion analytically. The existing knowledge for this flow region was obtained by observation and by numerical solution of the equations of motion. From photographic records (7) it is seen that the streamlines behind the cylinder widen out when R increases. At a certain

stage, flow separates from the cylinder and the wake appears. Inside the wake, there is a flow reversal along the symmetric axis and flow in the general direction of motion in the outer portions. These two standing eddies are bounded by the cylinder and separation lines. Keller and Takami (2) have calculated the streamlines of this flow at R = 4. Apelt (2) calculated the same flow at R = 40. Their results agree with Tietjen's (7) observations. The pressure distribution at the surface of the cylinder calculated by Apelt at R = 40 was close to that obtained by Thom (16). According to Taneda (2), wake first appears at R = 6 if the cylinder is circular. He also obtained a linear relationship between the relative wake length (length of the symmetric axis of the wake divided by the diameter of the circular cylinder), and the Reynolds number. As R increases the vortices become more and more elongated in the main flow direction. At certain critical Reynolds number, R_c, instability occurs and the wake begins to oscillate with an amplitude increasing downstream. The critical Reynolds number here is not a criterion for the transition from laminar flow to turbulent flow; instead, it divides two different ranges of laminar flow, - one of them is stable, the other is not. The value of R_c depends on the size of the obstacle relative to channel width (5), (14), the curvature of the body at the sides (3), the shape of the body (2) and the turbulence level in the main stream. The lower limit for R_c is about 30 (2).

As R increases beyond R_c the two standing eddies become asymmetric and oscillate in the lateral direction. Some rotating

fluid is shed at the end of every half period alternately from each side of the cylinder. The closed wake behind the cylinder breaks down. The fluid passing close to the cylinder appears to gather itself into discrete lumps, arranged in two regular staggered rows on each side of the cylinder. Most of the vorticity in the wake is concentrated in these lumps. All lumps in each row have vorticity of the same sign. This flow pattern is known as Karman's vortex street. The two oscillating eddies immediately behind the cylinder are not clearly recognizable when R is much above 100 (2), even though a vortex street continues to form in the wake up to much larger R. Far downstream from the cylinder, the rotation of these lumps of fluids is damped out by the surrounding fluid through viscous stresses.

For still higher Reynolds number (150 to 10,000 in Roshko's experiment (11)), the wake can be thought of as being composed of two parts. One is the region just behind the obstacle in which the vortex motion is obvious. The other is the region far downstream where the flow is essentially turbulent. Between these two regions there is a transition zone.

Fage and Johansen (4) studied vortex motion in the near-zone in detail. Vortex layers generated by flat plates, aerofoils, circular cylinders, wedges and ogival shapes for R between 1500 and 4500 were examined. The outer and inner boundaries of the vortex layers were defined as the line passing through the points of maximum and minimum velocities across the shear layer. The motion is steady near the bodies for the region near the inner boundary of the shear layer. The pressure on the outer boundary is

slightly larger than that in the inner region directly behind the obstacle. Owing to the inflow from both boundaries, vorticity spreads in the lateral direction, too. The simple expression

$$\frac{V_1^2 - V_2^2}{2U^2}$$

gives a close estimation of the total amount of vorticity passing a section of the vortex street per unit of time in which V_1 and V_2 are velocities at the outer and inner boundaries of the shear layer and U is the approach velocity. The spatial mean rate of the dimensionless vorticity transport for flat plates, circular cylinders, wedges and ogival shapes is 1.05, 0.96, 0.86, and 0.66 respectively. Therefore, the flat plate is the most effective shape to produce wake. The variation of velocity across the shear layer and the rate of increase of the width of the shear layer in the downstream direction are functions of body shape also. As a rule, a body with a greater front area has a thicker shear layer. As for the vortex sheet, both the frequency and the longitudinal spacing of the individual vortex in the rows depend on the spacing between the two layers of vortices instead of the shape of the body (4).

Roshko studied the transition zone (11). He believed that the laminar-turbulent transition always occurs in the vortex layers which separate from the obstacle before they break down. Thus each vortex passing downstream is composed of turbulent fluid. The mechanism is shown in Figure 4.

The position where transition takes place depends on R, on the roughness of the obstacle and on the main stream turbulence

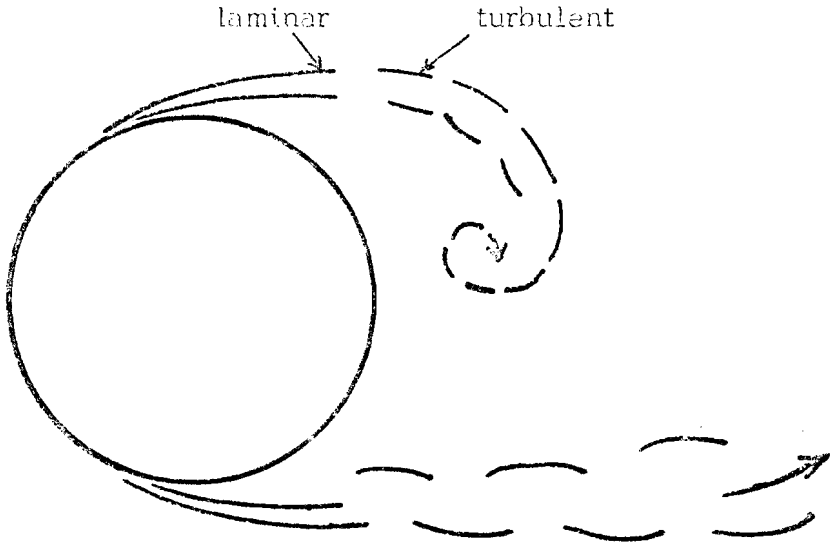

Figure 4. Flow transition inside shear layer

level. For a given roughness of the obstacle, the transition position moves toward the separation point when R and/or turbulence level increase, and will stay there until the boundary layer itself becomes turbulent. If the boundary layer is turbulent, the whole vortex layer is composed of turbulent fluid and no transition exists. As the transition point moves upstream, the vortex layers move much closer together and the vortices are dissipated in a much shorter downstream distance. After the turbulent transitions, the lumps of turbulent rotating fluid diffuse as they move downstream and are eventually obliterated. According to Roshko's data, the wake becomes fully turbulent 40 to 50 cylinder diameters downstream.

Townsend (18) also studied the flow in the same range of Reynolds number. He found that fully turbulent flow occurs only at the core of the wake. In the remaining region, the flow is only intermittently turbulent. Local pressure fluctuations inside the turbulent core cause billows of turbulent fluid to be emitted outward

from the fully turbulent core. Due to the adverse pressure gradient in the downstream direction, this transverse flow of turbulent fluid becomes weaker and weaker. Townsend inferred that in the transition zone the billows of turbulent fluid are responsible for the turbulent momentum transfer, whereas the diffusion of turbulent energy is carried out by the bulk movement of billows. It is believed that the zone studied by Townsend was downstream of that studied by Roshko; however, both zones were within the transition zone.

According to Townsend (19), the rapid development and stabilization of the turbulent flow occurs at least 100 cylinder diameters downstream. The microscale of turbulence is approximately constant over a large part of the width of the wake. The statistical distribution in time of the velocity components is near Gaussian except that of streamwise turbulent velocity at the extreme edge of the wake. Due to the turbulent kinetic energy transport across the wake, the turbulent intensity in the lateral direction is considerably larger than that in other directions. By considering the ratio of the kinetic energy of the main flow and that of the turbulent motion, he found that the complete dynamical similarity in the wake does not occur closer to the cylinder than 1000 cylinder diameters. Partial stability occurs about 100 diameters downstream for the characteristics of the mean flow, but this is not reflected in the turbulent field, which remains in transition. In the final state, because of turbulent kinetic energy dissipation, the turbulent motion is small compared with the mean flow. The ratio of kinetic energy associated with the mean flow and kinetic energy associated with the turbulent motion approaches 4.5 in the

limit. When Reynolds number exceeds 500,000 the boundary layer becomes fully turbulent before it separates from the obstacle and the entire wake is turbulent.

Free Streamline Theory

One way to obtain the approximate boundary of the wake zone is to employ free streamline theory. The problem to be considered is two-dimensional steady flow at large Reynolds number bounded partly by solid wall and partly by free streamlines of unknown shape and location on which certain assumptions about pressure distribution are made. The wake is considered as the exterior of the entire potential flow. The fact that the shape and location of the free streamline is unknown makes the problem very difficult, except in the case of a rigid boundary formed by a series of straight segments on which the separation point is fixed and is known.

The complex potential $\omega(z)$ is defined as

$$\omega(z) = \phi(x,y) + i\psi(x,y)$$

The real and imaginary part of the analytical function provides the velocity potential and stream function for the flow.

Conformal mapping is used in this theory. No matter what the physical z plane is, the ω plane is always considered to have a flow net that consists of a rectangular grid parallel to the ϕ and ψ axes. Hence, the flow in the plane is that of an infinite uniform flow in the negative ϕ direction. The lines of ϕ = constant and ψ = constant in the z plane remain as equi-

potential lines and streamlines. The particular configuration in the z plane depends on the mapping $\omega(z)$ defined in the flow region.

The velocity hodograph is the transformation from the z plane onto the $W = -\frac{d\omega}{dz} = u - iv$ plane. Such a transformation is useful in this type of problem where the separation layer occurs and where the boundary of the layer is not known a priori. The hodograph can be constructed based on physical observation of velocity or pressure distribution along the shear layer(2), (6).

Kirchhoff assumed that the fluid within the wake is everywhere at rest and at uniform pressure equal to that at infinity. From Bernoulli's theorem, the velocity of fluid on the separation line must be uniform and is equal to the approach velocity.

When this assumption is applied to the case where the wake was generated by a flat plate placed normal to the flow, the hodograph is simply a semi-circle, since along the solid boundary the direction of velocity is known as parallel to the wall. On the free streamline, the magnitude of velocity is assumed with direction left unknown. After taking the natural logarithm of the inverse of the hodograph, the flow boundary in the z plane is represented by a straight-sided figure or a generalized polygon. Then by applying the Schwartz-Christoffel theorem and by successive transformations, an expression for z in terms of ω can be obtained by integration. The transformation details can be found in most fluid dynamics textbooks such as Reference (15).

Roshko's Notched Hodograph Method

The assumption in Kirchhoff's free streamline theory is far from realistic and his theoretical results did not conform with experimental measurements. Roshko improved the theory by assuming the velocity along the free streamline to be constant but of higher magnitude than the free stream velocity. He assumed the velocity along the streamline was equal to the velocity at the separation point. According to the principle of conservation of energy, the velocity of fluid far downstream on the free streamline must decrease to the speed far upstream. Roshko accomplished this by suddenly reducing the velocity at infinite downstream to its far upstream value. The notched hodograph shown in Figure 5 is the result of this assumption. This can be done, as described in Chapter 3, because the shear layer diffuses rapidly and the idea of free streamline extending to infinity is unrealistic. Hence details of the free streamline at infinity are not important.

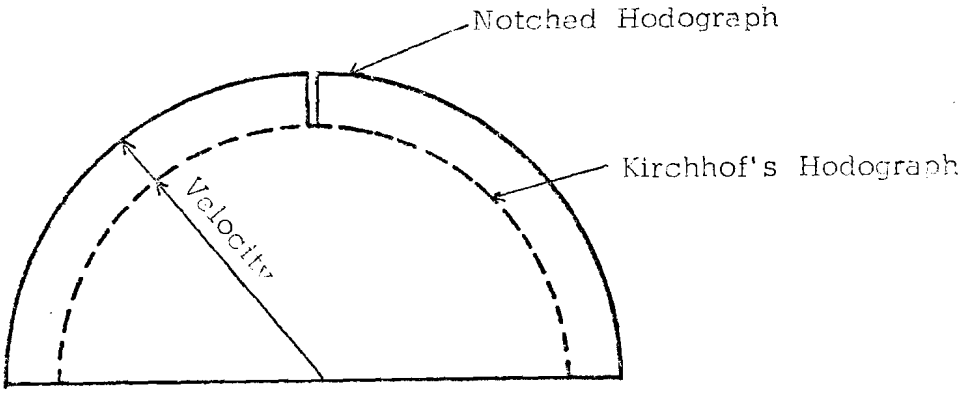

Figure 5. Roshko's notched hodograph.

The details of this method can be found in Reference 12.

CHAPTER 4

THEORY

A new hodograph for the wake boundary behind a flat plate placed normal to the flow is developed in this chapter. Unlike the free streamline theory or Roshko's notched hodograph, this model allows velocities along the shear layer to vary and hence, is more realistic for water wake in open channels.

The first part of this chapter is devoted to formulating the problem, the solution then follows.

Formulation of the Problem

By observation, it is assumed that:

1. The wake area is separated from the main flow by separation lines.
2. The flow exterior to the wake is inviscid and irrotational.
3. The flow exterior to the wake is steady.

The first assumption can be justified by noting that the thickness of the shear layer confining the wake is negligible compared to the extent of the flow. The rolling up and the mixing of the trailing vortices is not of interest to this investigation.

The second assumption can be justified by noting that viscous effects occur only in the very thin shear layer and that

layer is already idealized as a separation line. Also, the flow boundary is convergent so the flow outside the viscous layer can be considered as ideal potential flow.

The third assumption can be defended by noting that except near the wake, the flow is steady. Unsteadiness is caused near the wake by the rough water surface. Since it is confined to the thin shear layer, it can be neglected.

Under these assumptions, the fluid velocity $\bar{W} = u + iv$ is derived from a potential $\phi(x,y)$ and $\bar{W} = -\nabla\phi$ The function ϕ satisfies the Laplace equation

$$\nabla^2\phi = 0 \tag{1}$$

The boundary conditions are:

1. On the solid surface $S(x,y) = 0$, the normal component of the fluid velocity relative to the boundary S is zero,

$$\frac{DS}{Dt} = 0 \tag{2}$$

2. On the separation line $F(x,y) = 0$, there are two conditions which have to be satisfied. First, along the free surface of the boundary, the fluid particles must remain on the free streamline,

$$\frac{DF}{Dt} = 0 \tag{3}$$

Secondly, the velocities along the separation boundary change in a certain way defined implicitly by the hodograph,

$$W = W(z) \tag{4}$$

The problem now is expressed by the Laplace equation (1) together with boundary conditions described in equations (2), (3), and (4) above. Equation 4 is not known a priori.

The Solution

Since the flow is irrotational, both the stream function ϕ and velocity potential ψ exist. The complex potential is defined as follows:

$$\omega = \phi + i\psi \tag{5}$$

Since ω is an analytic function of $z = x + iy$, it follows that

$$-W = \frac{d\omega}{dz} = \frac{\partial\phi}{\partial x} + i\frac{\partial\psi}{\partial x}, \text{ thus}$$

$$W = u - iv \tag{6}$$

where W is the complex velocity, the conjugate of true velocity. Here the sign convention used is

$$u = -\frac{\partial\phi}{\partial x} \quad \text{and} \quad v = -\frac{\partial\psi}{\partial y}$$

The transformation of the region of flow from the physical z plane onto the W plane is called the velocity hodograph. The utility of the hodograph stems from the fact that, although the shape of the separation line is not known initially in the z plane, in the W plane its hodograph can be completely defined by other considerations not related to free streamline theory.

The ω plane is always considered to have a flow net that consists of a rectangular grid parallel to the ϕ and ψ axis. The flow represented by the ω plane is an infinite uniform flow in the negative ϕ direction. Both families of ϕ = constant and ψ = constant can be mapped onto the physical z plane by an analytic function $\omega = f(z)$; and the lines ϕ = constant and ψ = constant are still equipotential lines and streamlines in the z plane. The purpose

of the hodograph is to help determine the unknown function f. As long as a hodograph can be constructed based on experimental data or other information and at the same time if a transformation mapping the hodograph onto a simple polygon can be found, it is a straightforward process to apply the Schwarz-Christoffel transformation to find the function f, (15). Finally, both ϕ and ψ can be determined in the physical plane through integration. This process is applied to the wake of a flat plate as follows.

Suppose a stream of infinite width and velocity U encounters a fixed plate BB' of width 1 placed normal to the flow. Choose the center A of the plate as the origin. The streamline which strikes the center of the plate at point A will divide, follow the plate to B and B', thence follow along the separation lines BC and B'C' to infinity, as shown in Figure 6. The complete coordinate system is shown in Figure 7.

Suppose the dividing streamline is $\psi = 0$ and assume that $\phi = 0$ at point A, then $\phi = -\infty$ at C_∞ and C'_∞. After specifying the values of ϕ and ψ in the z plane, the configuration of the flow boundary in the ω plane is as shown in Figure 8. It is a simple polygon whose boundaries are $C'_\infty B'ABC_\infty$, and its interior is the cut ω plane; the interior angle at point A is 2π. By the Schwarz-Christoffel transformation, this polygon and its interior can be mapped onto the upper half of the ζ plane, making B'A,B correspond to $\zeta = -1, 0, 1$ respectively. (See Figure 9).

This transformation is accomplished as follows:

$$\frac{d\omega}{d\zeta} = \hat{K}(\zeta+1)^{\pi/\pi - 1}\ (\zeta-0)^{2\pi/\pi - 1}\ (\zeta-1)^{\pi/\pi - 1}$$

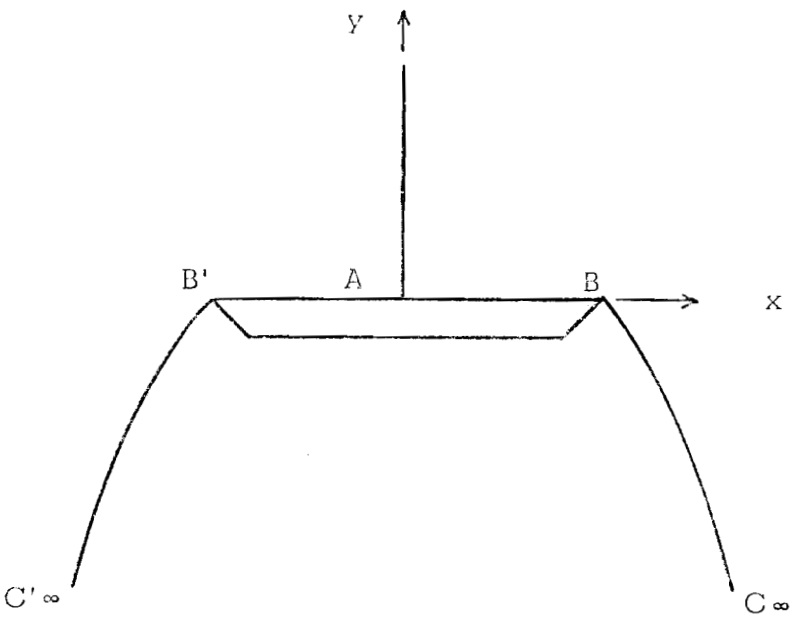

Figure 6. The physical z plane.

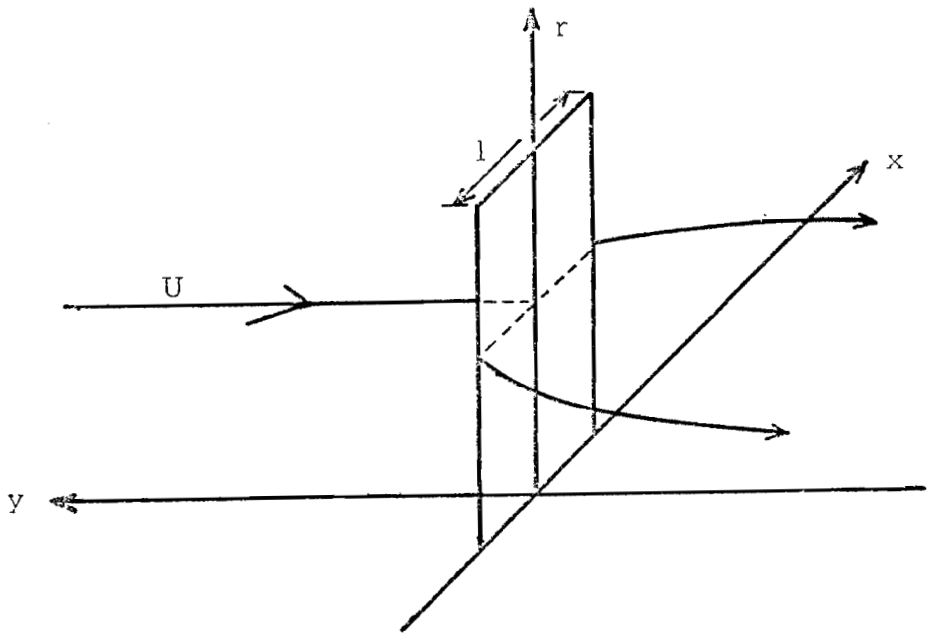

Figure 7. Coordinate system.

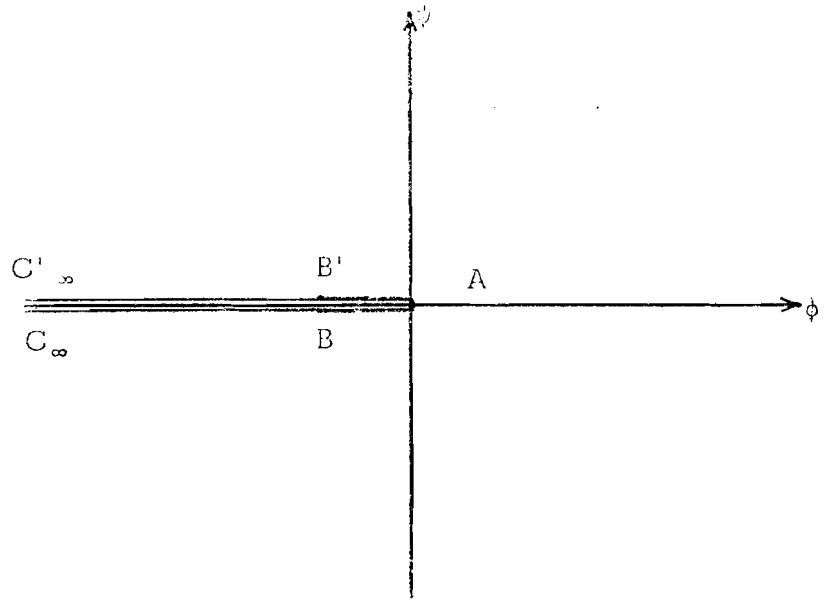

Figure 8. ω plane.

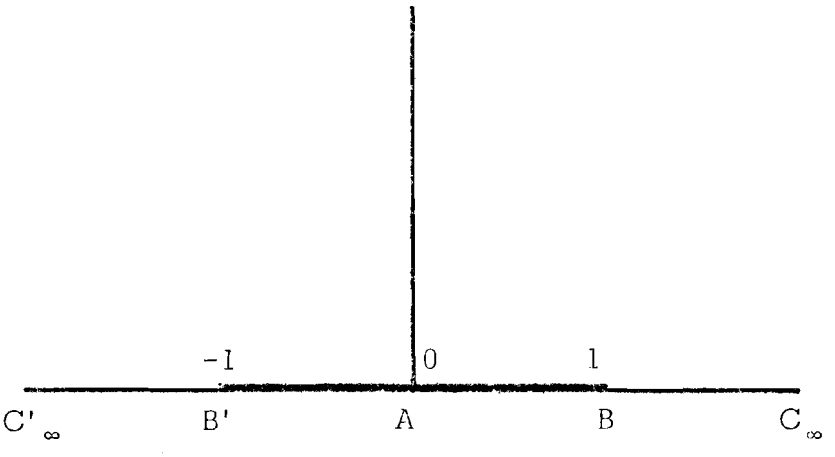

Figure 9. Intermediate ζ plane.

$$= \hat{K}\,\zeta \qquad ;\ \hat{K} = \text{constant}$$

$$\omega = \hat{K}\int \zeta\, d\zeta + e' \qquad ;\ e' = \text{constant}$$

$$= \frac{\hat{K}}{2}\,\zeta^2 + e'$$

Since $\omega = 0$, at $\zeta = 0$, the constant e' is zero.

Therefore,

$$\omega = \frac{\hat{K}}{2}\,\zeta^2 \tag{7}$$

where the constant $\hat{K}$ has the following physical meaning:

$$\hat{K} = 2\,|\,\phi(B)\,|\,e^{-i\,\Pi}$$

$$= 2\,\phi(B)$$

which is equal to twice the potential at B.

Now the hodograph needs to be constructed. The velocity along $S(x,y) = 0$ has known direction and the magnitude of velocity at point A is zero because A is the stagnation point. At the end point of S, or the separation point, the velocity has an unknown magnitude with its direction parallel to the plate. However, its magnitude can be measured experimentally. Actually the separation point is the starting point of the free streamline $F(x,y) = 0$. Therefore, in order to construct the hodograph, only the variation of velocity along the free streamline F is needed. As a matter of fact, to solve the problem, boundary condition 4 must be specified.

Looking at the flow in the vicinity of the plate, the water surface rises to its maximum height at the stagnation point A and drops a finite amount at the separation point. After the separa-

tion point the water surface keeps dropping parabolically up to the point where the shear layer starts to break and rolls up. For the flat plate, this occurs about one and one half plate widths downstream from the plate. The velocity at this point is observed as parallel to the approaching velocity. The flow is shown in Figure 10.

Figure 10. Flow in the vicinity of the plate.

It is seen from the picture that due to the drop of water surface, velocities along the shear layer are not equal to the approach velocity. It may be either lower or higher than the approach velocity and may change from point to point. In order to eliminate the constant velocity restriction in the free streamline theory, the hodograph shown in Figure 11 was assumed.

The hodograph is an off-centered circle defined by the following equation:

$$|W|^2 = u^2 + v^2 = 2\alpha'(-v) + \beta'; \quad \alpha'\beta' \neq 0, \ \beta' > 0, \quad v < 0 \quad (8)$$

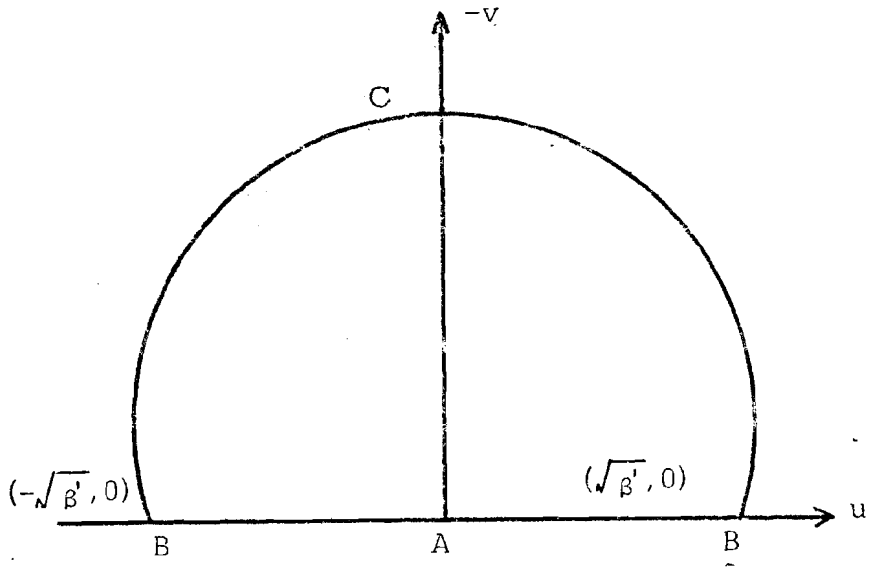

Figure 11. The hodograph

in which α' and β' are two constants with dimension L/T and $(L/T)^2$ respectively. The physical meaning of β' is expressed as follows:

when $-v = 0$ $\quad u = \sqrt{\beta'}$, the velocity at the separation point. (9)

The assumed hodograph is substituted for the unknown boundary condition specified by Equation 4.

Divide Equation 8 by β'; the off-centered circle is then normalized,

$$\hat{u}^2 + \hat{v}^2 = 2\alpha'(-\hat{v}) + 1 \tag{10}$$

where $\hat{u} = \frac{u}{\sqrt{\beta'}}$, $\hat{v} = \frac{v}{\sqrt{\beta'}}$, $\hat{\alpha}' = \frac{\alpha'}{\sqrt{\beta'}}$

The dimensionless velocity components are $\hat{u}$ and $\hat{v}$.

The normalized hodograph is shown in Figure 12 as the T plane. The arc BCB' then is transformed on to an infinite horizontal strip in the P-plane by the mapping

$$P = \ln \frac{T - 1}{T + 1} \tag{11}$$

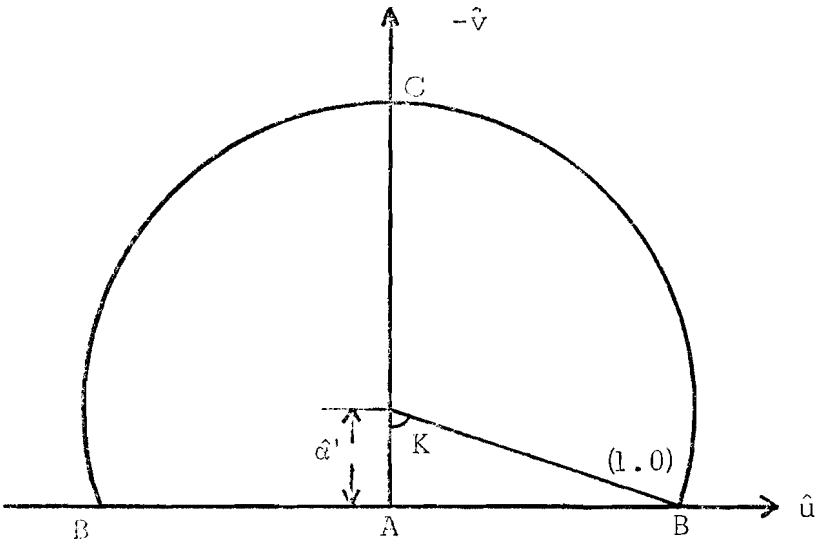

Figure 12. Normalized hodograph.

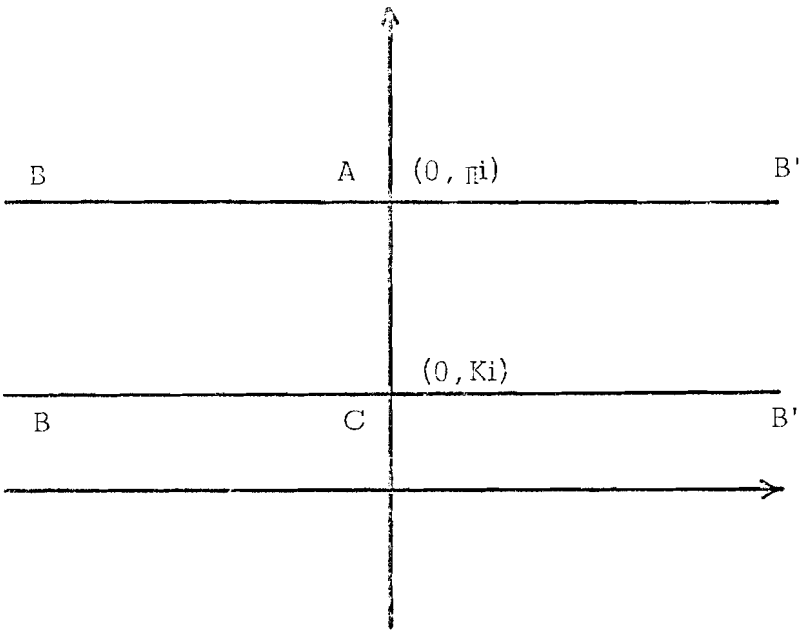

Figure 13. The intermediate P plane.

where in Figure 13, $K = \cot^{-1}\frac{\alpha'}{\sqrt{\beta'}}$. (12)

The next step is to transform the simple polygon in the P plane onto the upper half of the ζ plane, Figure 9, making B',A,B, correspond to $\zeta = -1$, 0, and 1 respectively.

By the Schwarz-Christoffel theorem

$$\frac{dP}{d\zeta} = K'(\zeta+1)^{\frac{0}{\Pi}-1}(\zeta-0)^{\frac{\Pi}{\Pi}-1}(\zeta-1)^{\frac{0}{\Pi}-1}, \quad K' = \text{constant}$$

$$P = K'\int\frac{d\zeta}{(\zeta+1)(\zeta-1)} + K'', \quad K'' = \text{constant}$$

$$P = \frac{K'}{2}\ln\frac{\zeta-1}{\zeta+1} + K''$$

When $P = Ki$, $\zeta \to \infty$, $K'' = Ki$

When $P = \Pi i$, $\zeta = 0$, $0 + \Pi i = \frac{K'}{2}[\Pi i - 0] + K''$, $K' = \frac{2(\Pi - K)}{\Pi}$

Therefore,

$$P = \frac{\Pi-K}{\Pi}\ln\frac{\zeta-1}{\zeta+1} + Ki \tag{13}$$

From Equation 11 and 13

$$\frac{\Pi-K}{\Pi}\ln\frac{\zeta-1}{\zeta+1} + Ki = \ln\frac{T-1}{T+1}$$

$$\ln\left(\left(\frac{\zeta-1}{\zeta+1}\right)^{\frac{\Pi-K}{\Pi}}e^{Ki}\right) = \ln\frac{T-1}{T+1}$$

$$\left(\frac{\zeta-1}{\zeta+1}\right)^{\frac{\Pi-K}{\Pi}}e^{Ki} = \frac{T-1}{T+1}$$

$$\frac{T-1}{T+1} - 1 = \left(\frac{\zeta-1}{\zeta+1}\right)^{\frac{\Pi-K}{\Pi}}e^{Ki} - 1$$

$$\frac{-2}{T+1} = \left(\frac{\zeta-1}{\zeta+1}\right)^{\frac{\Pi-K}{\Pi}}e^{Ki} - 1$$

$$\frac{T+1}{2} = \left[1 - \left(\frac{\zeta-1}{\zeta+1}\right)^{\frac{\Pi-K}{\Pi}} e^{Ki}\right]^{-1}, \quad T \neq \pm 1$$

$$\zeta \rightarrow T : T = 2\left[1 - \left(\frac{\zeta-1}{\zeta+1}\right)^{\frac{\Pi-K}{\Pi}} e^{Ki}\right]^{-1} - 1$$

But note that $T = W\sqrt{\beta'}$ therefore,

$$W = 2\sqrt{\beta'}\left[1 - \left(\frac{\zeta-1}{\zeta+1}\right)^{\frac{\Pi-K}{\Pi}} e^{Ki}\right]^{-1} - \sqrt{\beta'} \tag{14}$$

or,

$$-\frac{d\omega}{d\zeta} = 2\sqrt{\beta'}\left[1 - \left(\frac{\zeta-1}{\zeta+1}\right)^{\frac{\Pi-K}{\Pi}} e^{Ki}\right] - \sqrt{\beta'}$$

$$= \sqrt{\beta'}\left\{2\left[1 - \left(\frac{\zeta-1}{\zeta+1}\right)^{\frac{\Pi-K}{\Pi}} e^{Ki}\right]^{-1} - 1\right\} \tag{15}$$

From earlier results, Equation 7

$$\frac{d\omega}{d\zeta} = \frac{d\omega}{dz}\frac{dz}{d\zeta} = \hat{K}\zeta \tag{16}$$

substitute Equation 15 into 16,

$$\sqrt{\beta'}\left\{2\left[1 - \left(\frac{\zeta-1}{\zeta+1}\right)^{\frac{\Pi-K}{\Pi}} e^{Ki}\right]^{-1} - 1\right\}\frac{dz}{d\zeta} = \hat{K}\zeta \tag{17}$$

$$\frac{dz}{d\zeta} = -\hat{K}\left\{\sqrt{\beta'}\left\{2\left[1 - \left(\frac{\zeta-1}{\zeta+1}\right)^{\frac{\Pi-K}{\Pi}} e^{Ki}\right]^{-1} - 1\right\}\right\}^{-1}\zeta$$

$$z + c = \frac{-\hat{K}}{\sqrt{\beta'}}\int_a^{\zeta}\left\{2\left[1 - \left(\frac{\zeta-1}{\zeta+1}\right)^{\frac{\Pi-K}{\Pi}} e^{Ki}\right]^{-1} - 1\right\}^{-1}\zeta\, d\zeta \tag{18}$$

in which a and c are two constants.

The constant $\hat{K}$ can be determined by noting that the width of plate is 1; its end points B and B' correspond to $\zeta = 1, -1$ respectively.

Therefore,

$$1 = \frac{-\hat{K}}{\sqrt{\beta'}} \int_{-1}^{1} \left\{ 2 \left[1 - \left(\frac{\zeta - 1}{\zeta + 1} \right)^{\frac{\Pi - K}{\Pi}} e^{Ki} \right]^{-1} - 1 \right\}^{-1} \zeta \, d\zeta$$

or,

$$K = \frac{-\sqrt{\beta'} 1}{\int_{-1}^{1} \left\{ 2 \left[1 - \left(\frac{\zeta - 1}{\zeta + 1} \right)^{\frac{\Pi - K}{\Pi}} e^{Ki} \right]^{-1} - 1 \right\}^{-1} \zeta \, d\zeta} \tag{19}$$

After knowing $\hat{K}$, Equation 7 expressing ζ in terms of ω, the complex potential can be used, that is,

$$\zeta = \sqrt{\frac{2\omega}{\hat{K}}}$$

From Equation 15

$$z + b = \int_{d}^{\omega} \left\{ \sqrt{\beta'} \left\{ 2 \left[1 - \left(\frac{\zeta - 1}{\zeta + 1} \right)^{\frac{\Pi - K}{\Pi}} e^{Ki} \right]^{-1} - 1 \right\} \right\}^{-1} d\omega$$

$$= \frac{1}{\sqrt{\beta'}} \int_{d}^{\omega} \left\{ 2 \left[1 - \left(\frac{\sqrt{\frac{2\omega}{\hat{K}}} - 1}{\sqrt{\frac{2\omega}{\hat{K}}} + 1} \right)^{\frac{\Pi - K}{\Pi}} e^{Ki} \right]^{-1} - 1 \right\}^{-1} d\omega$$

Since along the separation line, $\psi = 0$, $\omega = \phi$. The equation for the free streamline can be obtained.

$$z + b = \frac{1}{\sqrt{\beta'}} \int_{d}^{\phi} \left\{ 2 \left[1 - \left(\frac{\sqrt{\frac{2\phi}{\hat{K}}} - 1}{\sqrt{\frac{2\phi}{\hat{K}}} + 1} \right)^{\frac{\Pi - K}{\Pi}} e^{Ki} \right]^{-1} - 1 \right\}^{-1} d\phi,$$

$$-\infty < \phi \leq 0$$

Let $d = \phi(B) = \frac{\hat{K}}{2}$ then $b = -\frac{1}{2}$

$$z = \frac{1}{\sqrt{\beta'}} \int_{\frac{\hat{K}}{2}}^{\phi} \left\{ 2 \left[1 - \left(\frac{\sqrt{\frac{2\phi}{\hat{K}}} - 1}{\sqrt{\frac{2\phi}{\hat{K}}} + 1} \right)^{\frac{\Pi - K}{\Pi}} e^{Ki} \right]^{-1} - 1 \right\}^{-1} d\phi + \frac{1}{2} \quad (20)$$

or, for $\phi < \frac{\hat{K}}{2}$

$$x = \frac{1}{\sqrt{\beta'}} \int_{\frac{\hat{K}}{2}}^{\phi} \frac{1 + E^{\frac{\Pi - K}{\Pi}}}{1 - E^{\frac{\Pi - K}{\Pi}}} d\phi + \frac{1}{2} \quad (21\text{-a})$$

$$y = 0$$

For $\phi > \frac{\hat{K}}{2}$

$$x = \frac{1}{\sqrt{\beta'}} \int_{\frac{\hat{K}}{2}}^{\phi} \frac{(1 - E^{\frac{2(\Pi - K)}{\Pi}})\, d\phi}{1 + 2E^{\frac{\Pi - K}{\Pi}} \mathrm{Cos}K + E^{\frac{2(\Pi - K)}{\Pi}}} + \frac{1}{2} \quad (21\text{-b})$$

$$y = \frac{-2}{\sqrt{\beta'}} \int_{\frac{\hat{K}}{2}}^{\phi} \frac{E^{\frac{\Pi - K}{\Pi}} \mathrm{Sin}K \, d\phi}{1 + 2E^{\frac{\Pi - K}{\Pi}} \mathrm{Cos}K + E^{\frac{2(\Pi - K)}{\Pi}}}$$

where

$$E = \frac{\sqrt{2\phi/\hat{K}} - 1}{\sqrt{2\phi/\hat{K}} + 1}$$

The equation of the separation line can also be obtained by combining Equations 18 and 19

$$z = 1 \frac{\int_{1}^{\zeta} \left\{ 2 \left[1 - \left(\frac{\zeta - 1}{\zeta + 1} \right)^{\frac{\Pi - K}{\Pi}} e^{Ki} \right]^{-1} - 1 \right\}^{-1} \zeta \, d\zeta}{\int_{-1}^{1} \left\{ 2 \left[1 - \left(\frac{\zeta - 1}{\zeta + 1} \right)^{\frac{\Pi - K}{\Pi}} e^{Ki} \right]^{-1} - 1 \right\}^{-1} \zeta d\zeta} + \frac{1}{2} \quad (22)$$

in which

$$0 < K = \mathrm{Cot}^{-1} \frac{\alpha'}{\sqrt{\beta_1}} < \Pi$$

In order to locate the free streamline, ζ is restricted to be real in Equation 22.

The alternative form of Equation 22 is

$$x = \frac{\int_1^{\zeta} \left\{ \left[1 - \left(\frac{\zeta-1}{\zeta+1}\right)^{\frac{2(\Pi-K)}{\Pi}}\right] \Big/ \left[1 + 2\left(\frac{\zeta-1}{\zeta+1}\right)^{\frac{\Pi-K}{\Pi}} \mathrm{Cos}K + \left(\frac{\zeta-1}{\zeta+1}\right)^{\frac{2(\Pi-K)}{\Pi}}\right] \right\} \zeta d\zeta}{\int_{-1}^{1} \left\{ \left[1 + \left(\frac{\zeta-1}{\zeta+1}\right)^{\frac{\Pi-K}{\Pi}}\right] \Big/ \left[1 - \left(\frac{\zeta-1}{\zeta+1}\right)^{\frac{\Pi-K}{\Pi}}\right] \right\} \zeta d\zeta} + \frac{1}{2} \qquad (23\text{-a})$$

$$y = -2 \frac{\int_1^{\zeta} \left\{ \left(\frac{\zeta-1}{\zeta+1}\right)^{\frac{\Pi-K}{\Pi}} \mathrm{Sin}K \Big/ \left[1 + 2\left(\frac{\zeta-1}{\zeta+1}\right)^{\frac{\Pi-K}{\Pi}} \mathrm{Cos}K + \left(\frac{\zeta-1}{\zeta+1}\right)^{\frac{2(\Pi-K)}{\Pi}}\right] \right\} \zeta d\zeta}{\int_{-1}^{1} \left\{ \left[1 + \left|\frac{\zeta-1}{\zeta+1}\right|^{\frac{\Pi-K}{\Pi}}\right] \Big/ \left[1 - \left|\frac{\zeta-1}{\zeta+1}\right|^{\frac{\Pi-K}{\Pi}}\right] \right\} \zeta d\zeta} \qquad (23\text{-b})$$

in which $\zeta \geq 1$.

The derivation of Equations 21 and 23 is given in Appendix A.

A numerical integration of Equation 23 was performed using the program listed in Appendix B. The trapezoidal rule was employed. The result is plotted in Figure 14.

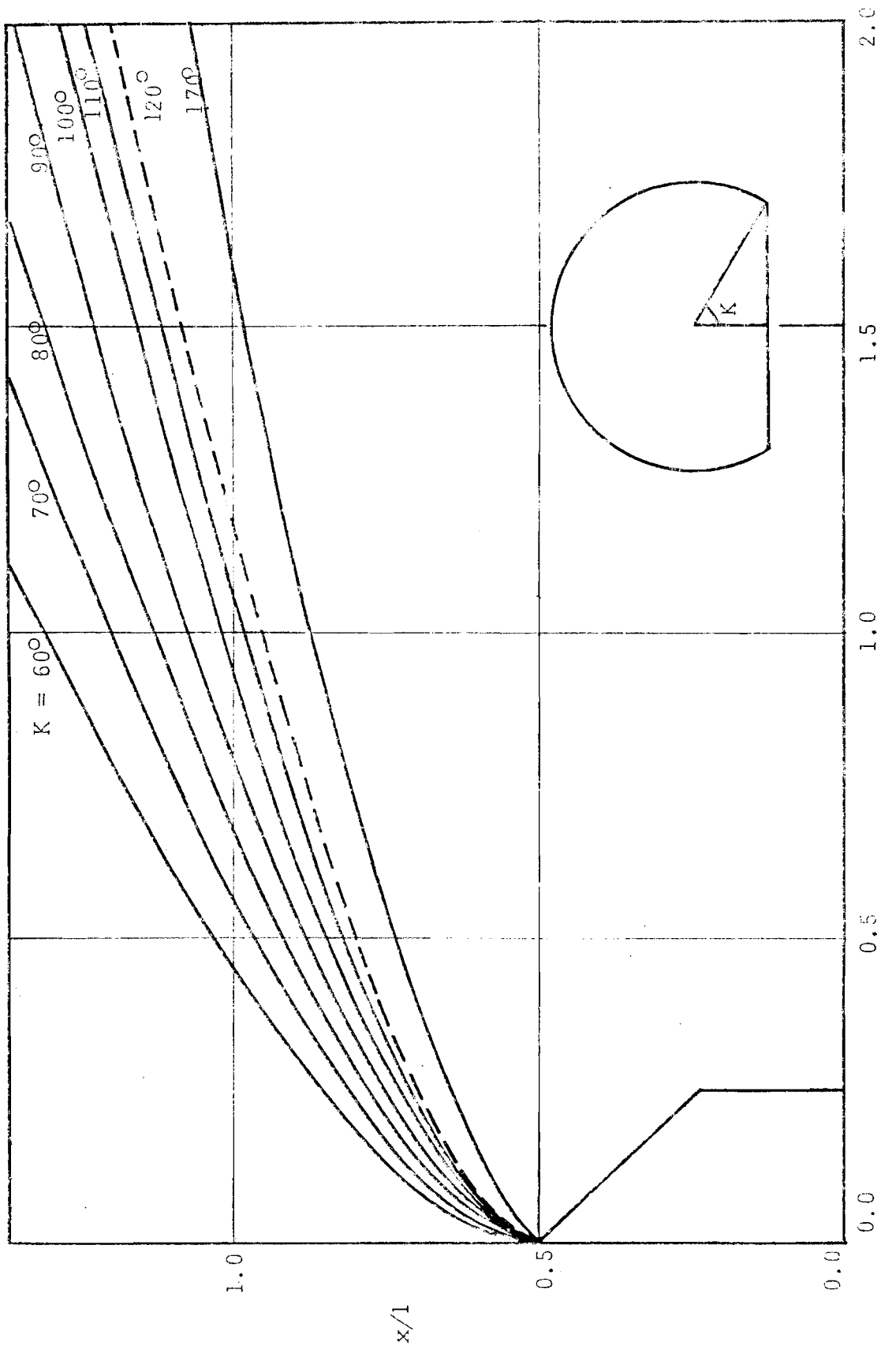

Figure 14. Theoretical wake boundaries.

CHAPTER 5

EXPERIMENTAL WORK

Actual wake boundaries were located in a straight open channel for the following purposes:

1. To verify the theoretical model for the wake boundary generated by a flat plate placed normal to the stream.
2. To investigate the effect of water surface on the wake boundary.
3. To compare the sizes of wake generated by a flat plate, ninety degree wedge and a circular cylinder.
4. To observe a general picture of the sizes of wake generated by an embedded sphere at three different degrees of submergence.

The apparatus used and experimental procedures are described in this chapter. The results are given in Chapter 6. Experimental data are included in the Appendix.

Apparatus

The experimental equipment consisted of a rectangular tilting flume supplied by a low volume centrifugal pump with an air activated regulating valve and an electromagnetic flow meter for flow measurement. The discharge could be adjusted be-

tween zero and 1400 gpm. The flume was 24 feet long and 1.5 feet wide with transparent side walls 2 feet high. The channel slope was adjustable with a hydraulic cylinder. The tailwater depth was controlled by the tail gate, operated by a hydraulic cylinder. Water temperature for all runs was approximately 75°F.

The obstacle under study was placed on a platform 9 inches high and 42 inches downstream from the head box. In order to eliminate the large vortex that occurred at the entrance of the platform, a triangular ramp was built in front of the platform to form a slowly converging floor so that the flow approaching the test section would be steady and uniform. Four layers of 0.5" x 0.5" metal mesh were inserted at the outlet of the head box to eliminate the large scale eddies produced inside the head box. Details of the test section and the obstacles are shown in Figure 15 and Figure 16 respectively.

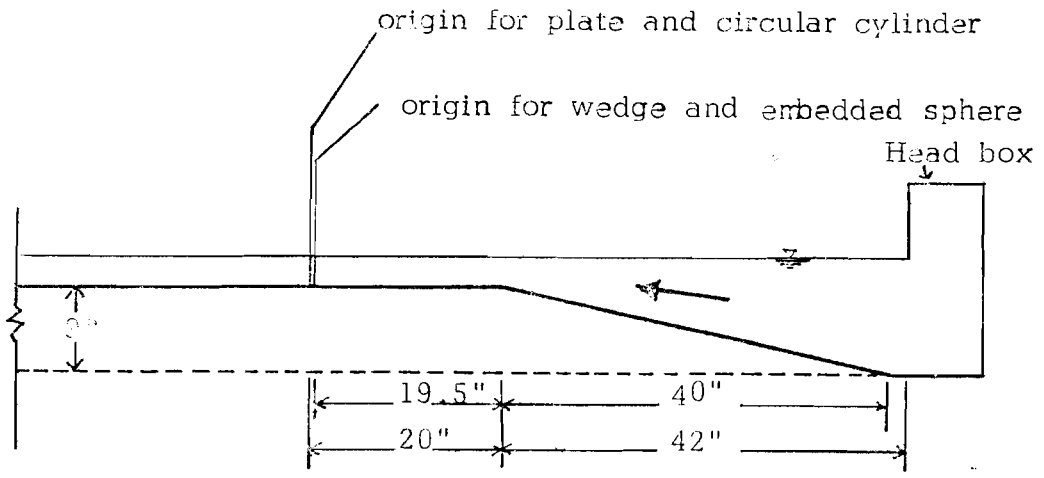

Figure 15. Channel geometry at the test section.

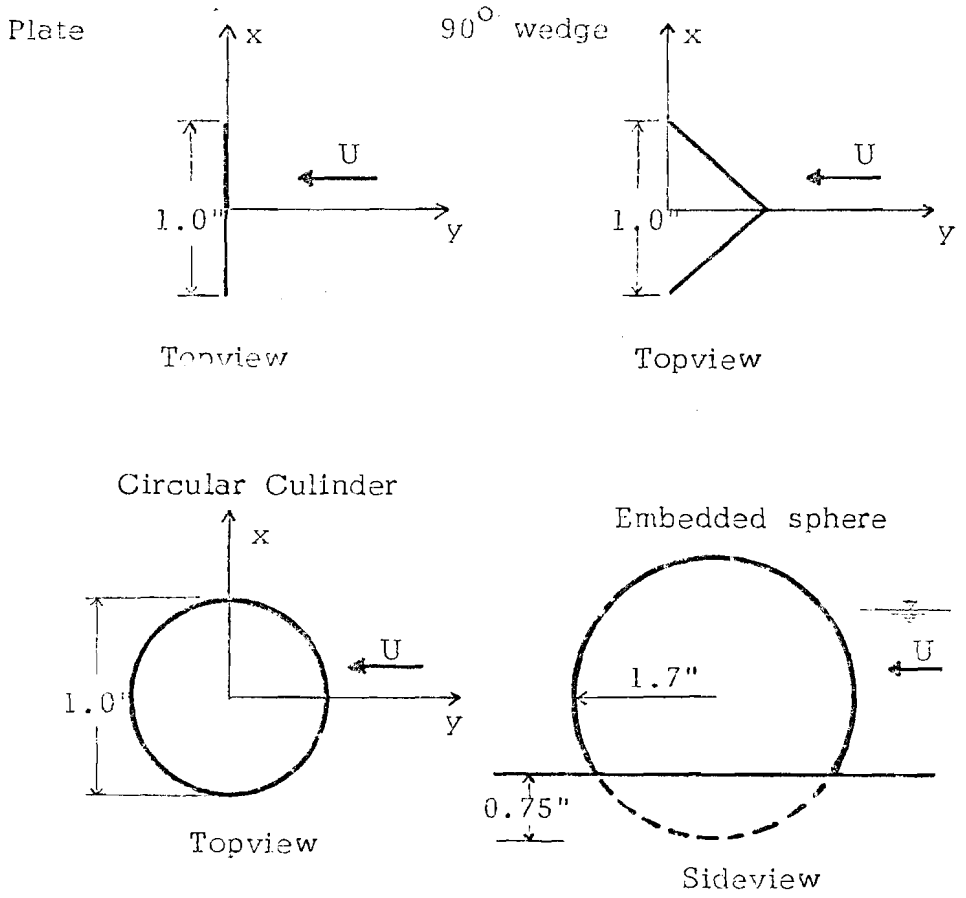

Figure 16. Details of Obstacles.

Both dye and a hydrogen bubble device were used to visualize the wake boundary. Dye was introduced at the front face of the plate through a small rubber tube (4 mm outside diameter). A series of holes 1 inch apart was drilled in the tube. The tube was positioned so that dye left the tube in a direction parallel to the face of the plate or perpendicular to the approaching velocity. The tube was placed in the stagnation zone so that the flow was not

seriously disturbed. Figure 17 shows the dye injection device and the approximate wake boundary.

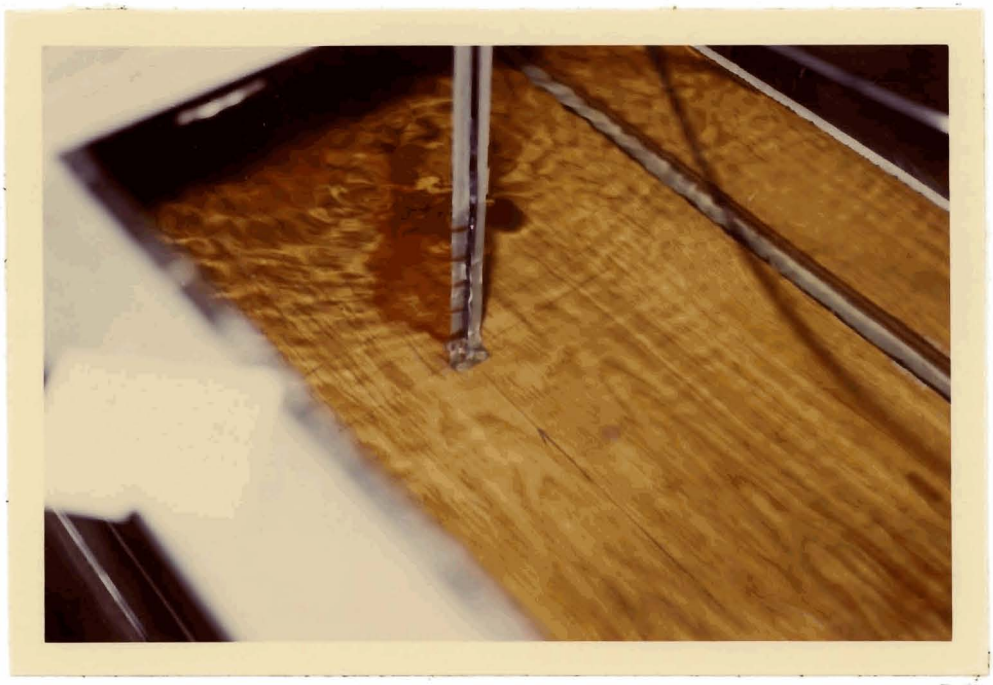

Figure 17. Dye injection device and the marked wake boundary.

The hydrogen bubble device is shown in Figure 18.

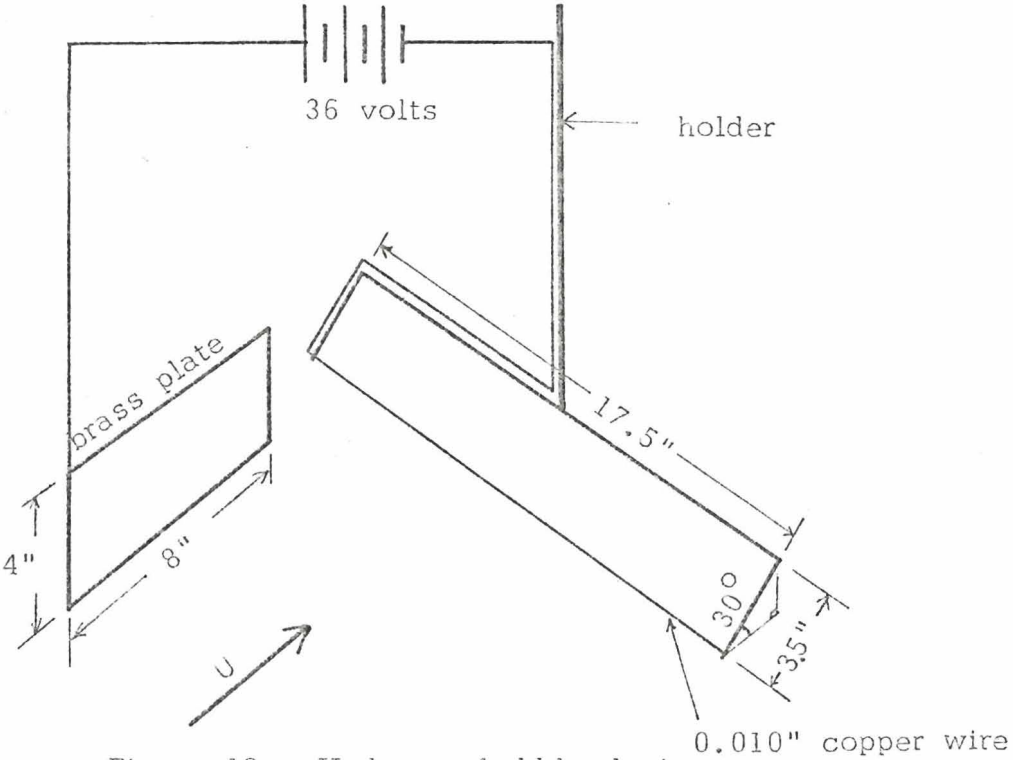

Figure 18. Hydrogen bubble device.

In order to see the tiny bubbles, the channel floor was painted black. Figures 2 and 19 are photographs illustrating the use of hydrogen bubble techniques.

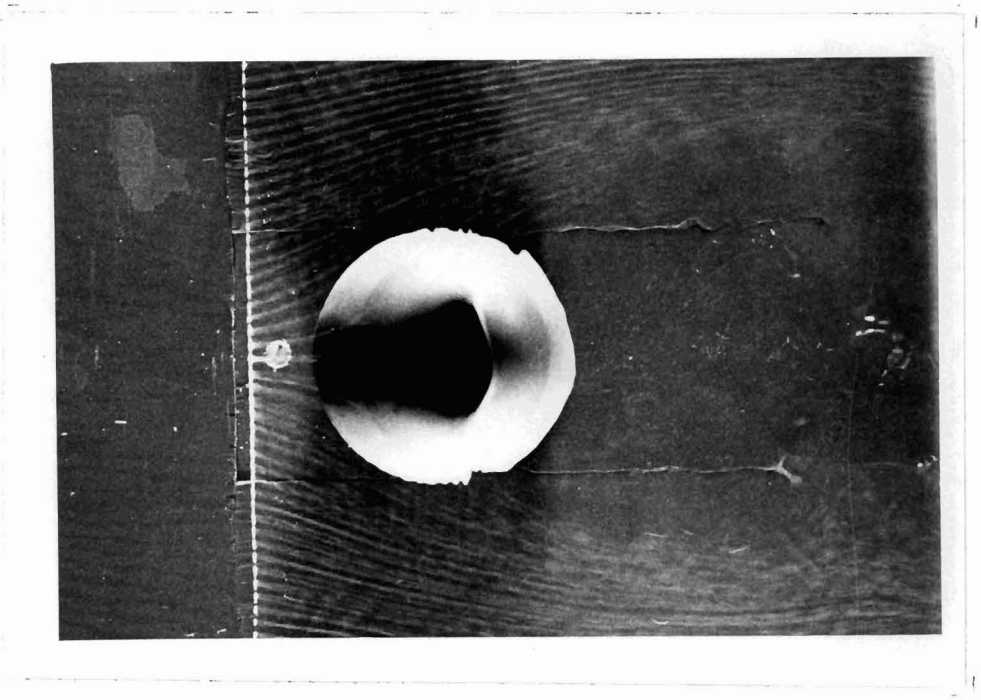

Figure 19. Visualization by hydrogen bubble.

Information could only be obtained using the dye or hydrogen bubble technique with a very low approach velocity where there was no significant drop of water surface behind the obstacle. When the velocity was higher, the water surface, disturbed by the obstacle, was so rough that the streamlines within the flow field could not be identified.

Quantitative results of the wake boundary were obtained by using yaw and pitch probes. These two probes were built to the dimensions specified in Reference 8. The tubes of each probe have a 3 mm. outside diameter.

The pressure differences among the three tubes of the probe were measured by two Model 7 Variable Reluctance Differential Pressure Transducers produced by the Validyne Engineering Co. The pressure sensing element for each transducer was an 0.1 psi flat diaphragm. The pressure difference across the diaphragm causes a displacement of the diaphragm. When the transducer is excited by the power supply of a recorder, an output voltage proportional to the pressure difference is produced.

This output voltage was recorded by a Beckman Type R Dynograph Recorder. The block diagram of the recorder is shown in Figure 20, and the entire setup is shown in Figure 21.

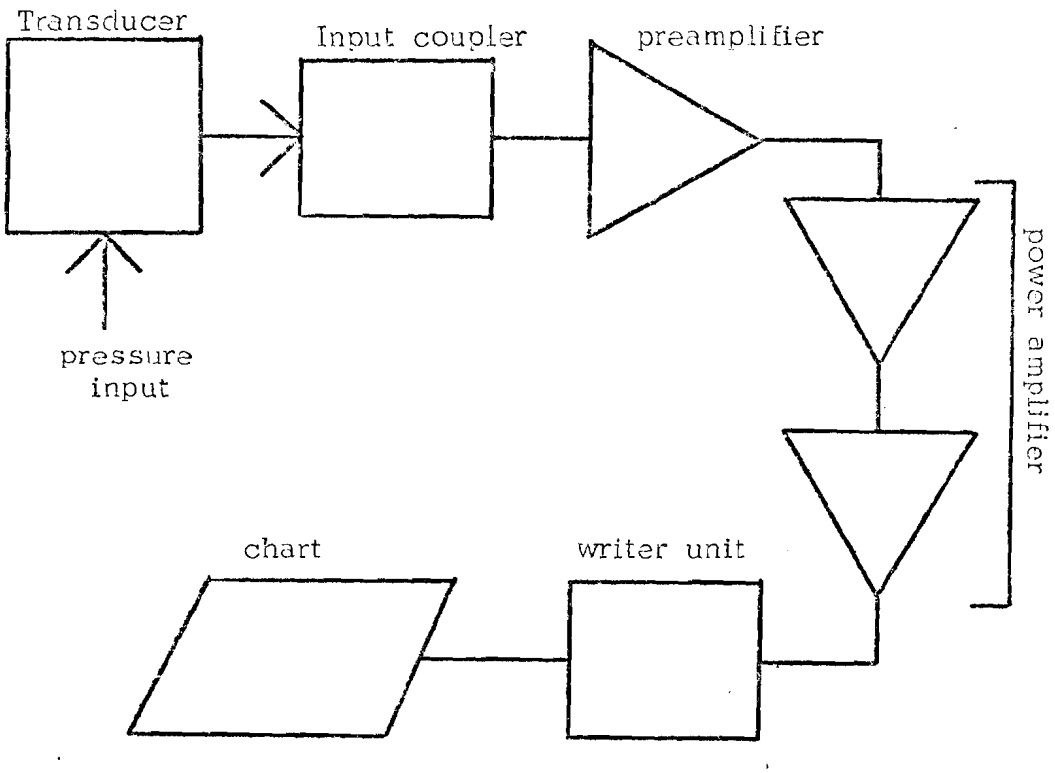

Figure 20. The block diagram of the Recorder.

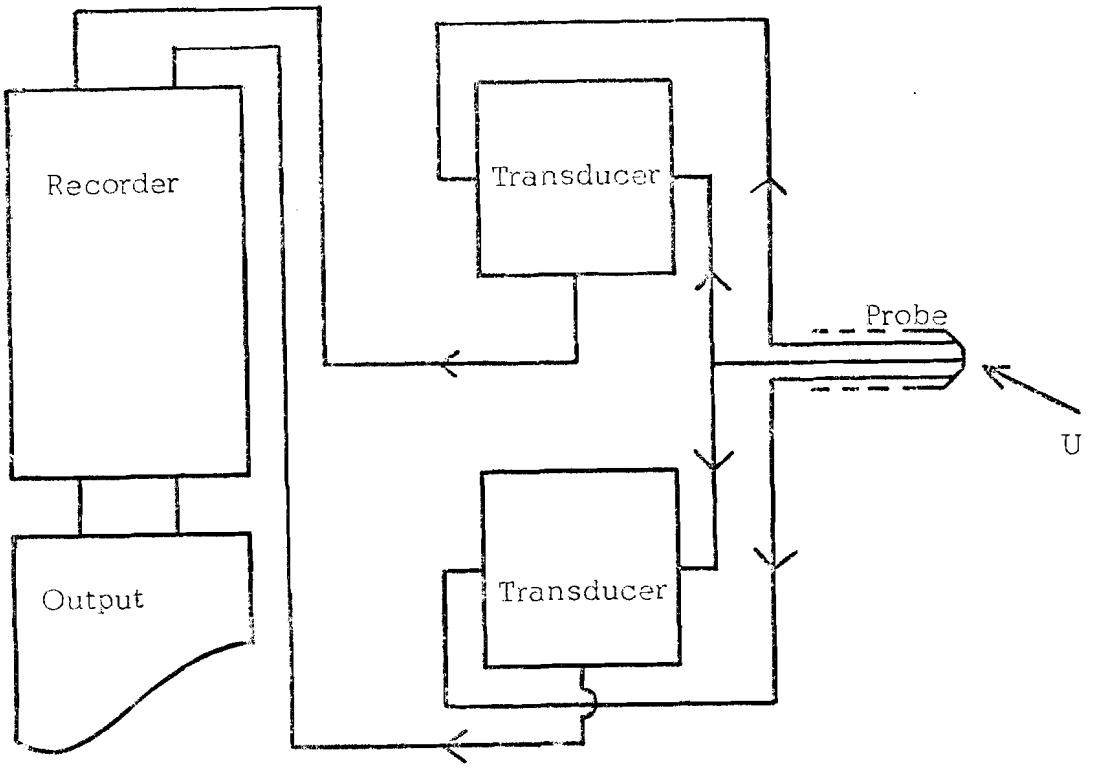

Figure 21. Schematic diagram for the pressure measurement.

Pressure Transducer and Recorder Calibration

The transducer and the recorder were calibrated together. After setting up the system and priming the transducer and tubes with water, the ends of the three tubes were submerged in a bucket containing water, and the pens of the writer unit of the recorder were centered to zero. Then, the two transducers were separated by clamping the common pressure tube. By doing so, the two channels can be calibrated one at a time.

The reference differential pressures were produced by setting the tube leading to the side hole of the probe at different elevations while maintaining the central tube at an arbitrary but fixed datum.

The elevation differences were read from a vertical scale with the help of a vernier accurate to 0.01 inch. This set up is shown in Figure 22.

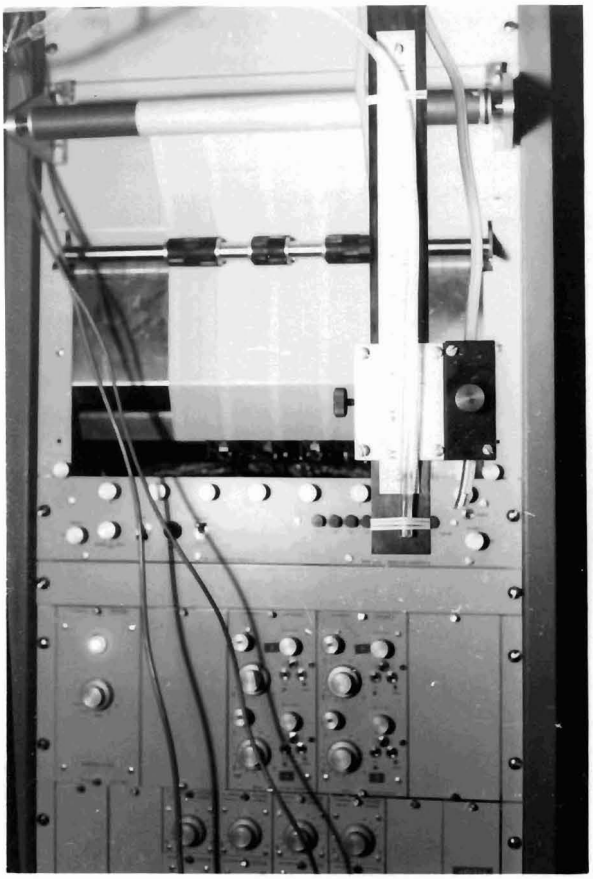

Figure 22. Calibration device for the transducer and the Recorder.

Figure 23 is an example of the output of calibration. Pen deflections were proportional to the pressure difference applied. The differential pressure in this study ranged from zero to 1.4 inches of water or from zero to approximately 0.05 psi.

The Use of Yaw and Pitch Probes

The yaw and pitch probes were constructed to the specifications proposed by Rajaratnam and Muralidhar (8). Calibration curves presented in this reference were used for the probes.

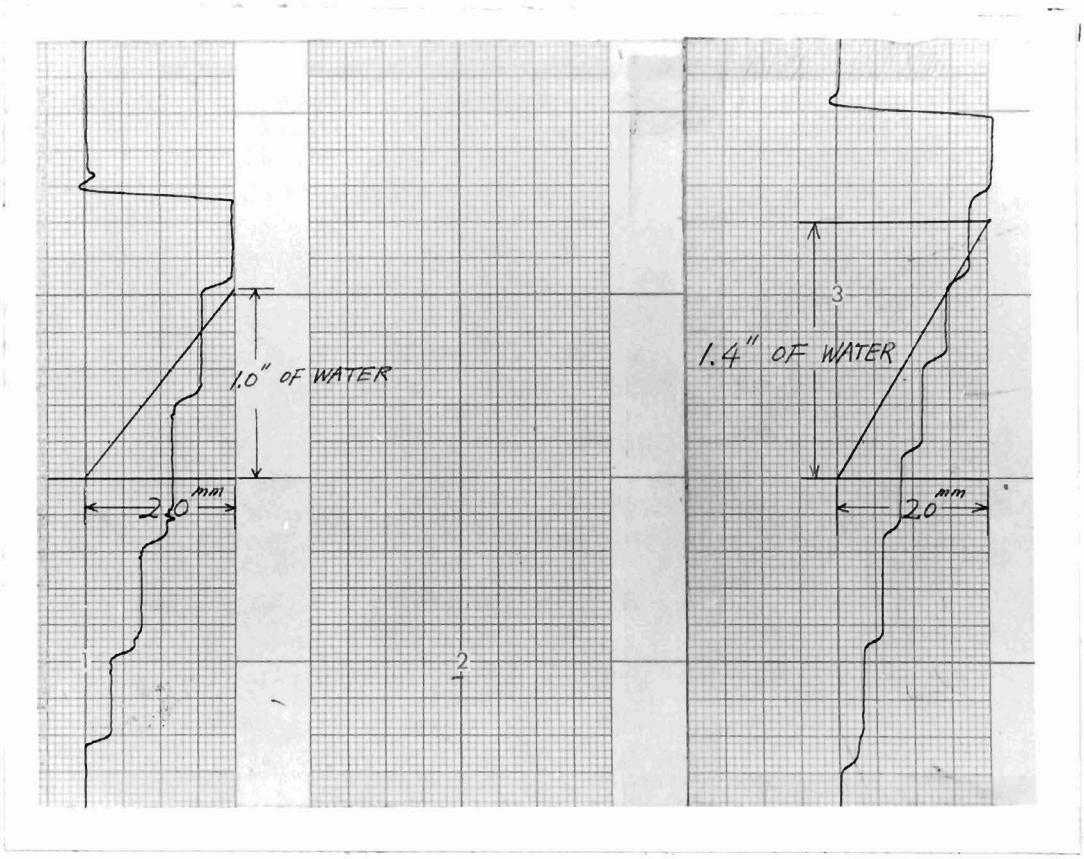

Figure 23. An example of the output during calibration.

At any point in a flow field the water velocity in the plane of the probe hits the probe with an angle α. The piezometric heads indicated by the three tubes of the probe are:

$$h_1 = h_0 + H_1\frac{V^2}{2g}$$

$$h_2 = h_0 + H_2\frac{V^2}{2g}$$

$$h_3 = h_3 + H_3\frac{V^2}{2g}$$

where H_1, H_2, and H_3 are calibration coefficients.

A tenth degree polynomial was used to interpolate Rajaratnam's and Muralidhar's data relating α to H in which H is equal to the ratio of $H_3 - H_2$ to $H_1 - H_2$. Similarly, another polynomial of 6th degree was used to interpolate the data relating α to H_6, where H_6 is another calibration coefficient. The magnitude of the

velocity is then computed from the expression:

$$V = H_6 \sqrt{2g(H_1 - H_2)}$$

Since,

$$H = \frac{H_3 - H_2}{H_1 - H_2} = \frac{P_3 - P_2}{P_1 - P_2}$$

The term H can be calculated directly from the pressure measurements. By employing the two polynomials, the magnitude and direction of the velocity can then be obtained. The coefficients of the two polynomials were calculated by POLRG, a core image program. Tables C-1 and C-2 in the Appendix C show the residue between the values estimated using the polynomials and the original data.

The computer program used to reduce the pressure measurement data is also included in Appendix C.

Measurement Procedure

The flume was horizontal for all experiment runs. After setting the discharge, the tail gate was adjusted until the water depth at the entrace of the testing section was three times the "diameter" of the obstacle. The "diameter" was defined as the widest dimension of the obstacle in the direction perpendicular to the approaching velocity. Measurements of the location of the wake boundary and the velocities at that point were made at 0.125, 0.25, 0.50, 0.75, 1.00, 1.50 and 2.00 diameters downstream from the obstacle.

The pitch probe was chosen for the basic measurements. The probe was slowly moved in the transverse direction starting at the

interior of the potential flow region and moving toward the wake. When the probe approaches the wake, it first senses a steep velocity increase and then indicates a sharp drop of velocity. This change was noted by watching the output of the recorder. When this occurred, the movement of the probe was stopped and its position was recorded. An example output for this purpose is shown in Figure 24.

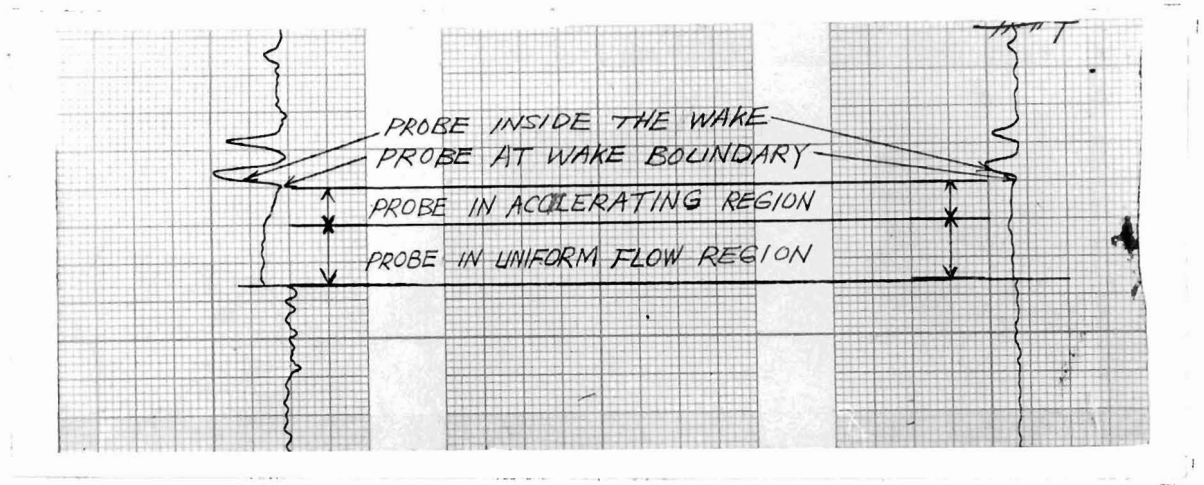

Figure 24. An example output for the location of the wake boundary.

After locating the wake boundary, the probe was reset for about twenty seconds to the position where maximum velocity occurred so that the pressure differences could be recorded over a period of time. Since the flow was turbulent, this step was necessary to obtain a mean velocity.

The probes are basically two dimensional, i.e., the yaw probe detects a horizontal angle correctly when properly oriented in the vertical plane and the pitch probe senses the correct vertical angle when properly oriented in the horizontal plane. Prior to positioning the pitch probe at each station, the horizontal angle

was measured approximately. Thus the pitch probe could be set to this predetermined horizontal angle and the wake boundary could be determined. A set of angle for one setup is shown in the following table.

Table 1.

STATION*	0.125	0.25	0.50	0.75	1.00	1.50	2.00
ANGLE	30^{o}	15^{o}	8^{o}	4^{o}	0^{o}	0^{o}	0^{o}

*The stations were expressed as the ratio of downstream distance to the diameter of the plate.

Figure 25 shows the pitch probe set at an appropriate angle.

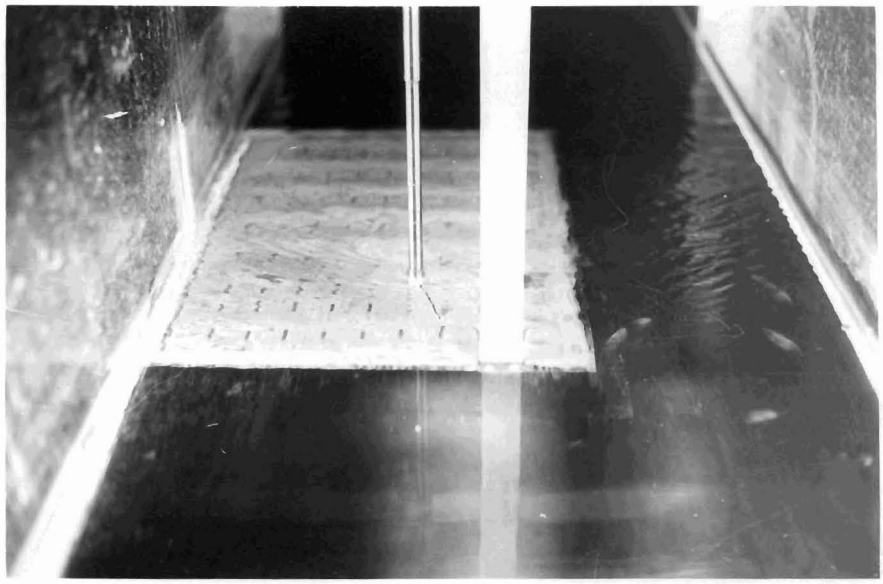

Figure 25. The angle of pitch probe relative to the flow.

Data were obtained for three different approach velocities for each obstacle.

CHAPTER 6

RESULTS AND DISCUSSIONS

Theoretical analysis of wake flow is discussed in this chapter together with comparisons with Kirchhoff's free streamline theory and the result obtained by previous experiment. After presenting the results of experimental work described in Chapter 5, theoretical and experimental results are compared and discussed. Suggestions for further study are given at the end of this chapter.

The Theory

The hodograph developed in this study does not explicitly bring the velocity far downstream back to the value at infinite upstream as required by the conservation of energy in ideal flow. For the real flow instead of extending the wake downstream to infinity, the shear layer breaks down about two diameters downstream and from that point the wake boundary is no longer clearly defined. Hence, it is meaningless to worry about the details of the shear layer at infinity. In addition, the fluid velocity at the breakdown point of the shear layer was observed as parallel to the approaching velocity. Should the velocity at this point equal that at infinity, the hodograph can be adjusted by choosing the proper K value to satisfy the principle of conservation of energy.

The dynamic boundary condition (Equation 4) is expressed in terms of velocity instead of pressure. It is simpler to work with velocity when using the hodograph method. The corresponding pressure variation along the separation line is related to the velocity through Bernoulli's equation.

In the derivation when progressing from Equation 22 to Equation 23, only the principle branch of the quantity $e^{i(2n+1)\pi}$ is used. Since the exponent is an irrational number, there exists an infinite number of solutions. Should the solution derived from the principle branch fail to predict the wake boundary, other solutions should be tried.

The parameter K cannot be determined by the theory itself. Instead, it must be determined from other considerations. For this study values of K were arbitrarily selected ranging from $K = 60^{\circ}$ to $K = 170^{\circ}$. The applicability and the goodness of fit to actually located wake boundary depends on the choice of the K value. (i.e. The proper K value could be obtained by superposition of derived wake boundaries over plots obtained experimentally.)

Comparisons with Kirchhoff's Solution and Existing Experimental Results

In the present theory if $K = 90^{\circ}$, the hodograph is a half circle. It is then identical to the hodograph in Kirchhoff's solution.

In Figure 26 the solution for $K = 90^{\circ}$ was plotted for comparison with Kirchhoff's solution (taken from reference 5). The two curves are identical except for plotting and computation errors. The lower dashed experimental curve (taken from the same reference), which

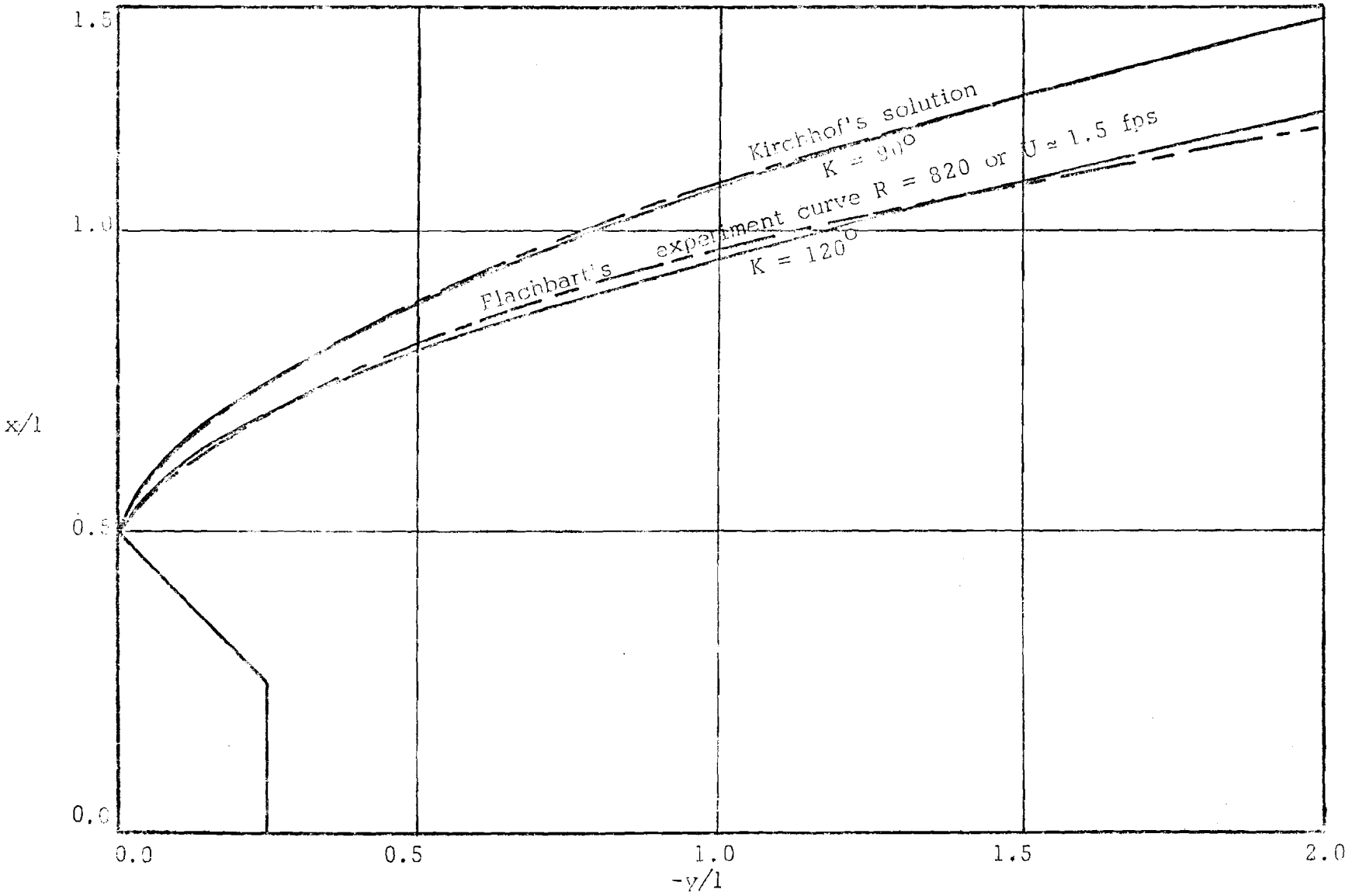

Figure 26. Comparison with Kirchhoff's solution and Flachbart's experimental result.

Kirchhoff's solution was intended to predict, is similar to the curve predicted by the present theory with $K = 120^{o}$. From this comparison, it can be seen that the present theory is more flexible or more general and comes much closer to predicting the actual location of the wake in real flow.

Experimental Results

It was observed that even though the obstacle is prismatic through the water depth, the resulting wake is actually three dimensional; wider at the bottom and narrower on the top. Figure 27 shows the wake boundaries at three different approach velocities. For each approach velocity, wake boundaries are given at three different elevations. This variation in width of wake as a function of depth becomes obvious when the approach velocity increases.

Figures 28, 29, and 30 compare the wake sizes of three different prismatic obstacles - namely, the flat plate, the 90-degree wedge and the circular cylinder. For the first two cases the separation points are fixed at the end of the obstacles. The direction of separation velocity at the separation point are similar and the wake of the plate is approximately equal to that produced by the wedge though the wedge wake is a little smaller. The separation point of the wake of the circular cylinder is not fixed at one point but moves back and forth and could not be accurately located. The left end of the dotted lines in these figures does not indicate the starting point of the shear layer but simply the first station where the shear layer could be located. The sizes of the

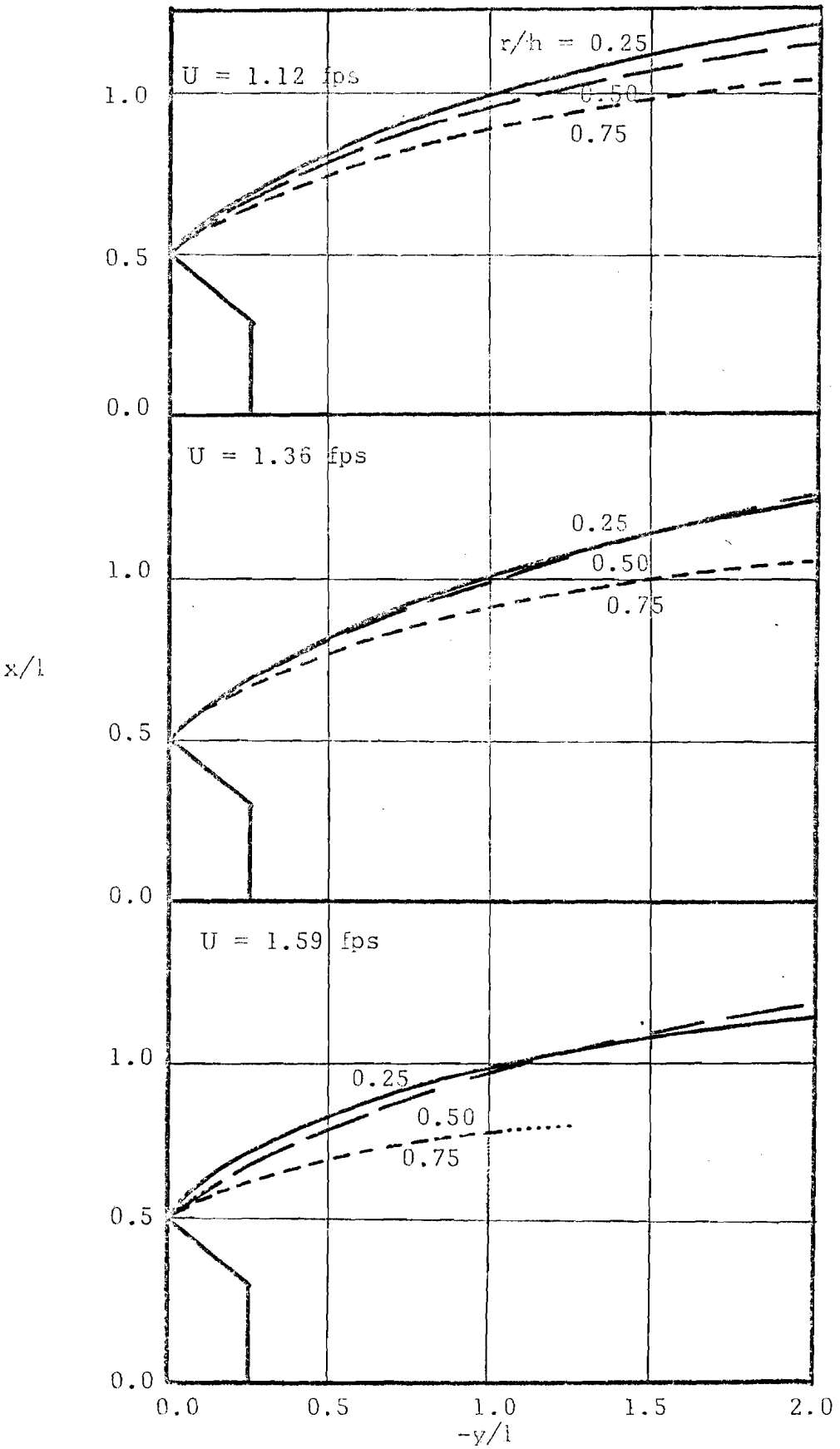

Figure 27. Wake size as a function of water depth r at h/l = 3.0.

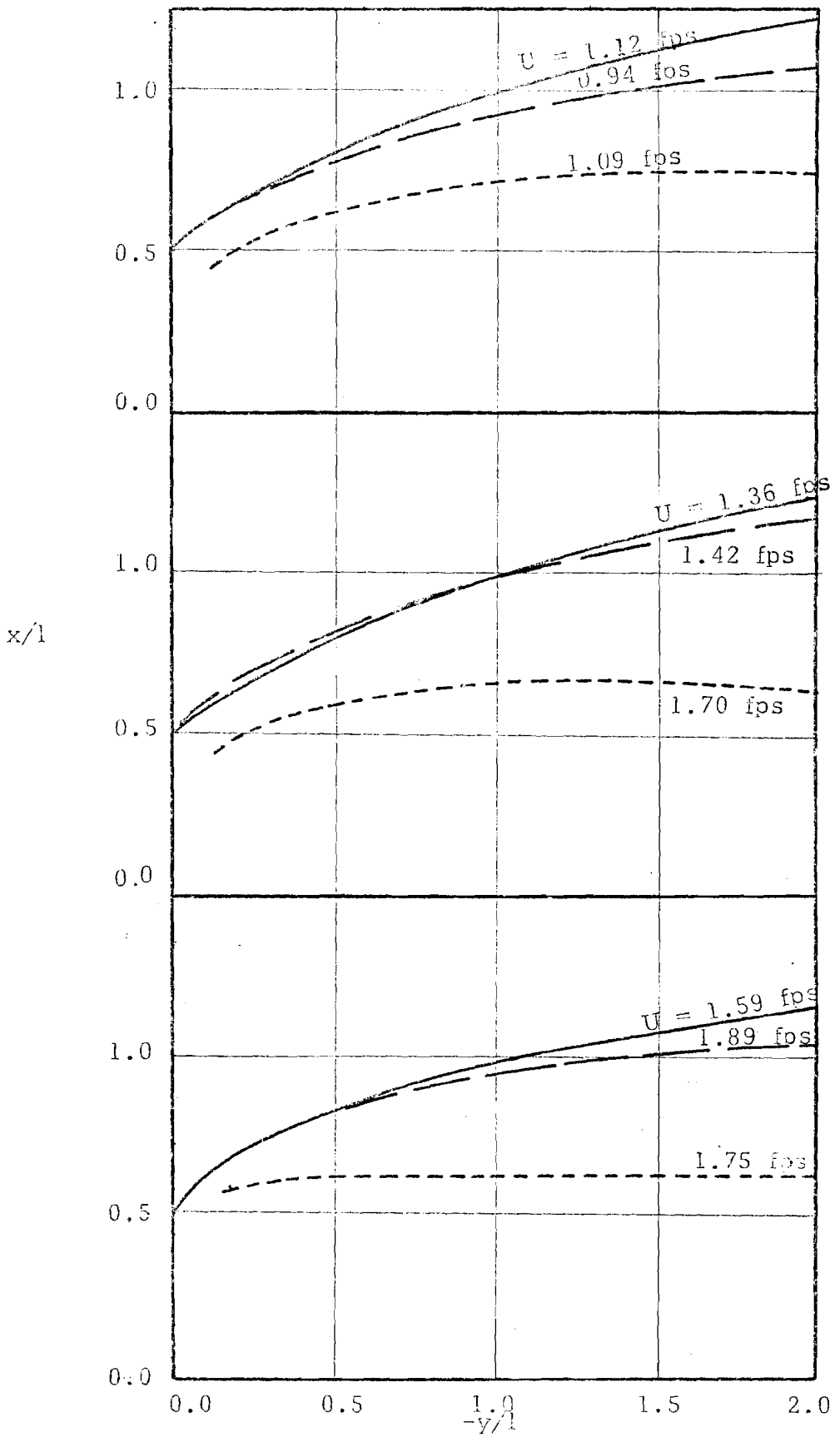

Figure 28. Wakes produced by plate (solid line), 90° wedge (dashed line), and circular cylinder (dotted line) at h/l = 3.0 and r/h = 0.25.

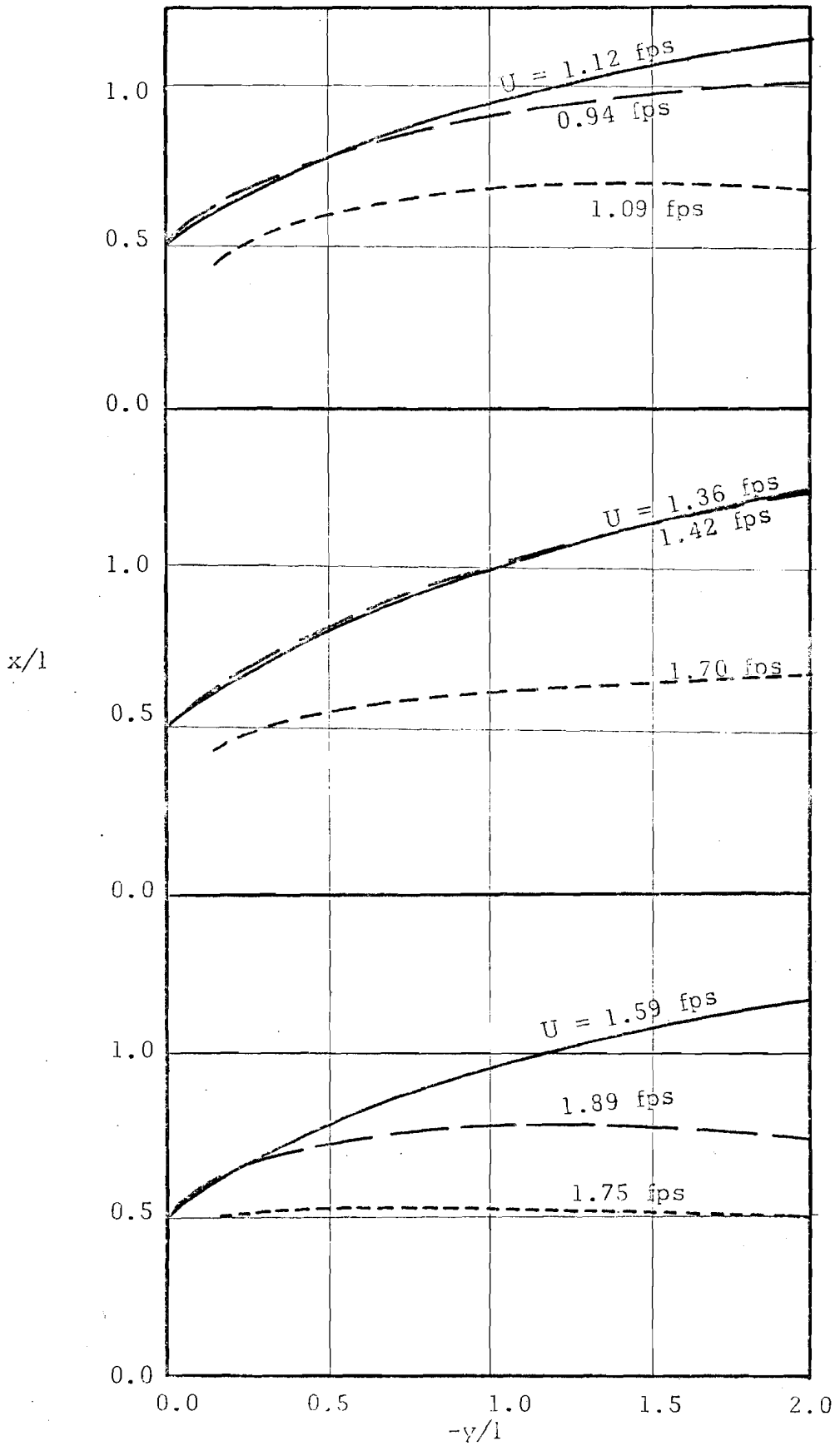

Figure 29. Wakes produced by plate (solid line), 90° wedge (dashed line), and circular cylinder (dotted line) at h/l = 3.0 and r/h = 0.50.

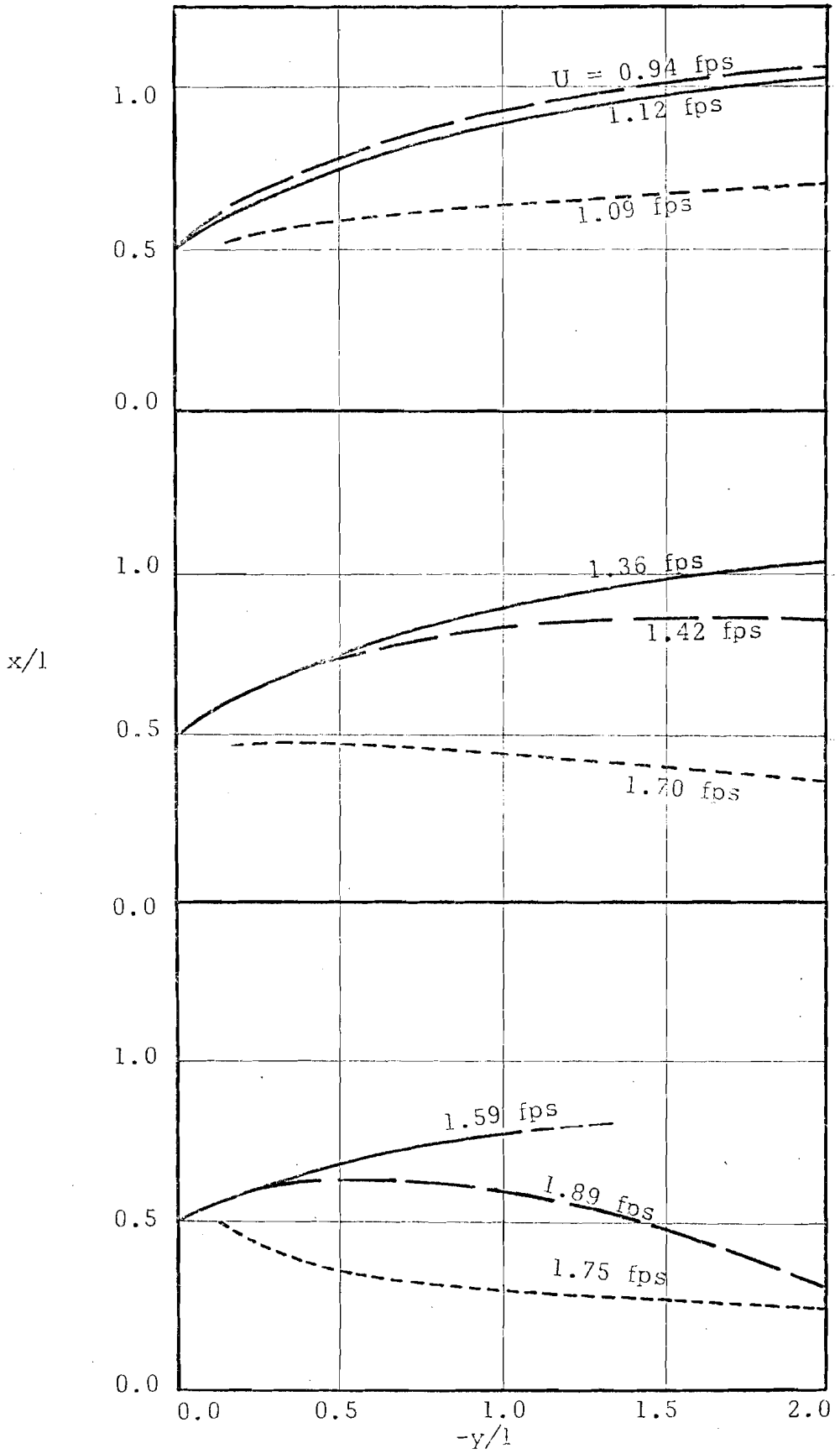

Figure 30. Wakes produced by plate (solid line), 90° wedge (dashed line), and circular cylinder (dotted line) at h/l = 3.0 and r/h = 0.75.

wake for the higher velocities are considerably smaller than for the lower velocities. The trend of the change of wake size with approaching velocity for the circular cylinder is similar to that for the plate in that the wake gets narrower at high approach velocities.

It is suspected that for different obstacles the tangent to the obstacle at the separation point is more important for the purpose of estimating the wake size; whereas the contact area between the potential flow and the obstacle is only important for estimating the thickness of the shear layer as stated in Reference 4.

Figure 31 shows the wake produced by an embedded sphere at three different degrees of submergence. For this specific embedded sphere when the ratio of approach water depth to sphere diameter is 0.5, the flow past the sphere is so shallow that measurements could only be made at $r/h = 0.25$. Since the water depth is small, the wake boundary measured at this elevation can be employed to estimate the whole wake size. The wake was observed as similar to the circular cylinder wake. With a depth/diameter ratio of 0.70, the wake widens considerably. The curvature of shear layer of the top portion is larger than those at the lower portion, and the wake is much wider near the top. For a depth/diameter ratio of 1.0, water flows over the top of the sphere. The wake is "closed" immediately downstream from the sphere. Since the separation point is not measurable due to the unsteadiness of the flow, the left end point of the curves does not indicate the starting point of the shear layer.

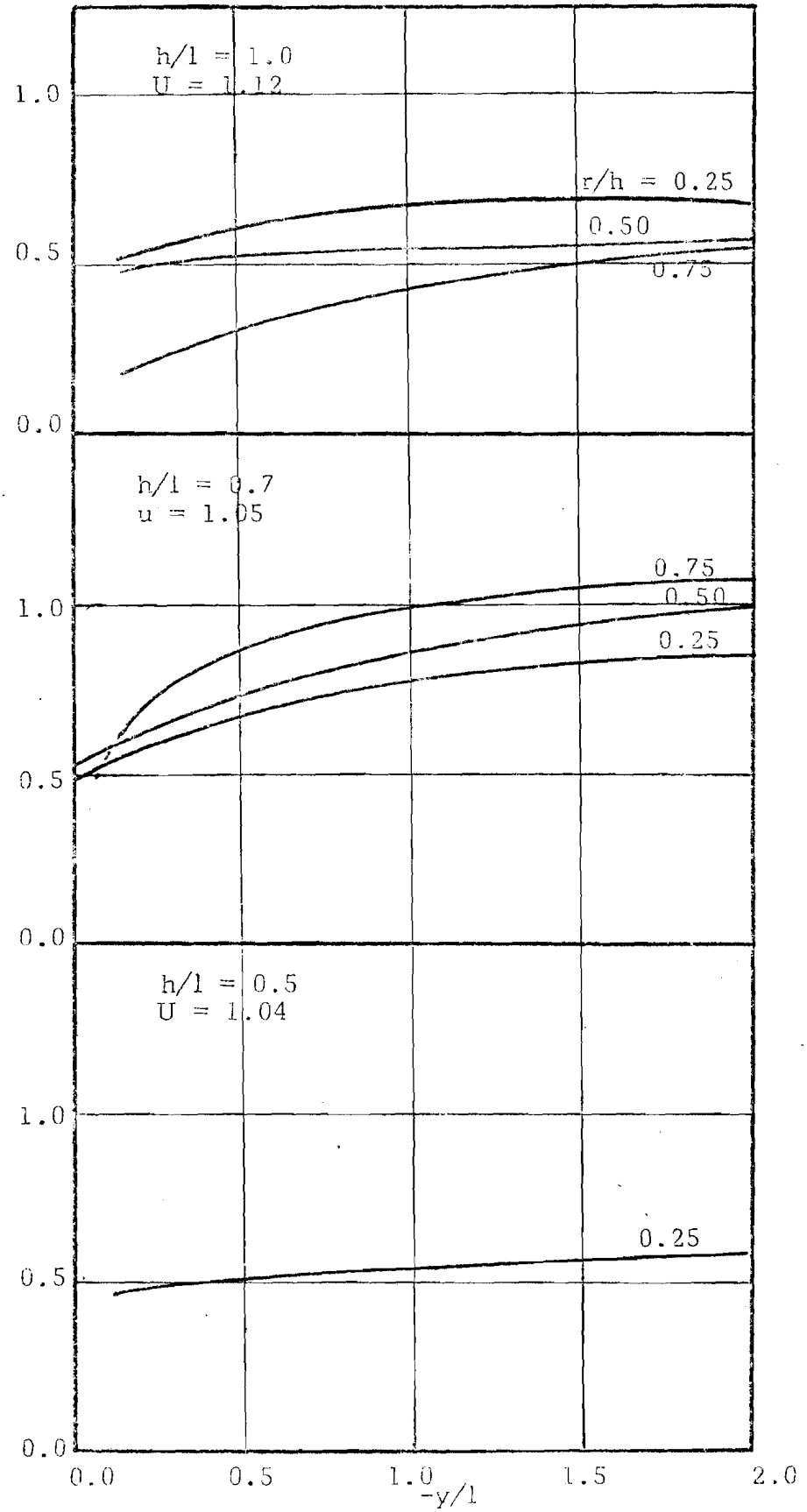

Figure 31. Sizes of wake produced by embedded sphere at different degree of submergence.

The following table gives the water surface elevation behind the sphere. By using this table together with Figure 31, a three dimensional plot of the wake can be made.

Table 2. Water surface elevation behind the embedded sphere.

Station (y/l)*	0.5 from symmetric axis	On the symmetric axis
	h/l = 0.5	
0.0	1.10"	/
0.5	1.01"	0.77"
1.0	0.91"	0.73"
1.5	0.94"	0.76"
2.0	1.10"	0.90"
	h/l = 0.7	
0.0	2.19"	/
0.5	2.06"	1.84"
1.0	2.02"	1.85"
1.5	2.02"	2.00"
2.0	2.09"	2.09"
	h/l = 1.0	
0.0	3.24"	3.24"
0.5	3.22"	2.91"
1.0	3.21"	3.18"
1.5	3.27"	3.18"
2.0	3.35"	3.28"

*The stations were expressed as the ratio of downstream distance to the diameter of the sphere.

The calibration curves of the yaw and pitch probes were developed from data in the potential core of a plane turbulent wall jet as explained in Reference 8. The velocities hitting the three

holes of the probe are identical. However, in this study when the probe is placed near or on the shear layer, the velocities hitting the holes are not uniform, i.e. there is a velocity gradient across the nose of the probe. Therefore, the measured velocities are doubtful. This defect was serious for the yaw tube, since the width dimension of the probe in the plane of the flow was about the same as the width of the shear layer. The probe width of the pitch probe was about one third the width of the shear layer. Based on this fact, the pitch probe was chosen to locate the wake boundaries. Before locating the wake boundary, it was necessary to know the direction of the velocity in the horizontal plane in the vicinity of the shear layer so that the pitch probe could be set to that angle. Unfortunately, the yaw tube measurement was the only means of estimating the direction of the velocity in the vicinity of the shear layer. Because of this difficulty, intensive measurement of the velocity in the shear layer immediately downstream from the obstacle could not be accomplished. Therefore, no useful information of velocity variation along the shear layer was obtained. Actually this kind of information is very hard to obtain since in addition to the need for a small three dimensional Pitot tube, the position of the probe has to be identified very accurately because of the velocity variation across the shear layer. However, should this kind of information become available, the assumption of the theory can be verified directly by superimposing the measured velocities on the hodograph and comparing theoretical and measured velocities.

Comparison Between the Developed Model of This Study and Experimental Observations; The Effect of Water Surfaces

By using Equation 23, the theoretical wake boundaries were calculated with different K values 10 degrees apart. One of them was then chosen in such a way that it best fit one of the experimental curves. These comparisons are shown in Figure 32 through Figure 34. In each figure the solid lines are theoretical lines with the appropriate K value shown on each line. In general the theoretical wake boundaries agree with those actually located in the flume. The exception is the case where the shear layer is near the water surface and the approach velocity is high. Two trends of the change of the parameter K are noted. First, at the same velocity, K increases from the channel bottom to the water surface with an increasing rate. Secondly, at a fixed elevation relative to the channel bottom, K increases when the approach velocity increases.

The flow approaching the test section is uniform in each dimension; whereas after it passes the plate, the flow is no longer uniform in the direction. Therefore, the flow must be treated as an infinite number of horizontal layers. The theory can then be applied to each of these horizontal layers of two-dimensional flow. For all experimentally measured wake boundaries, the K value for the theoretical curves which best fit the measured curves, were well above 90 degrees.

No examples of three-dimensional wakes generated by a prismatic obstacle in the presence of a free water surface were

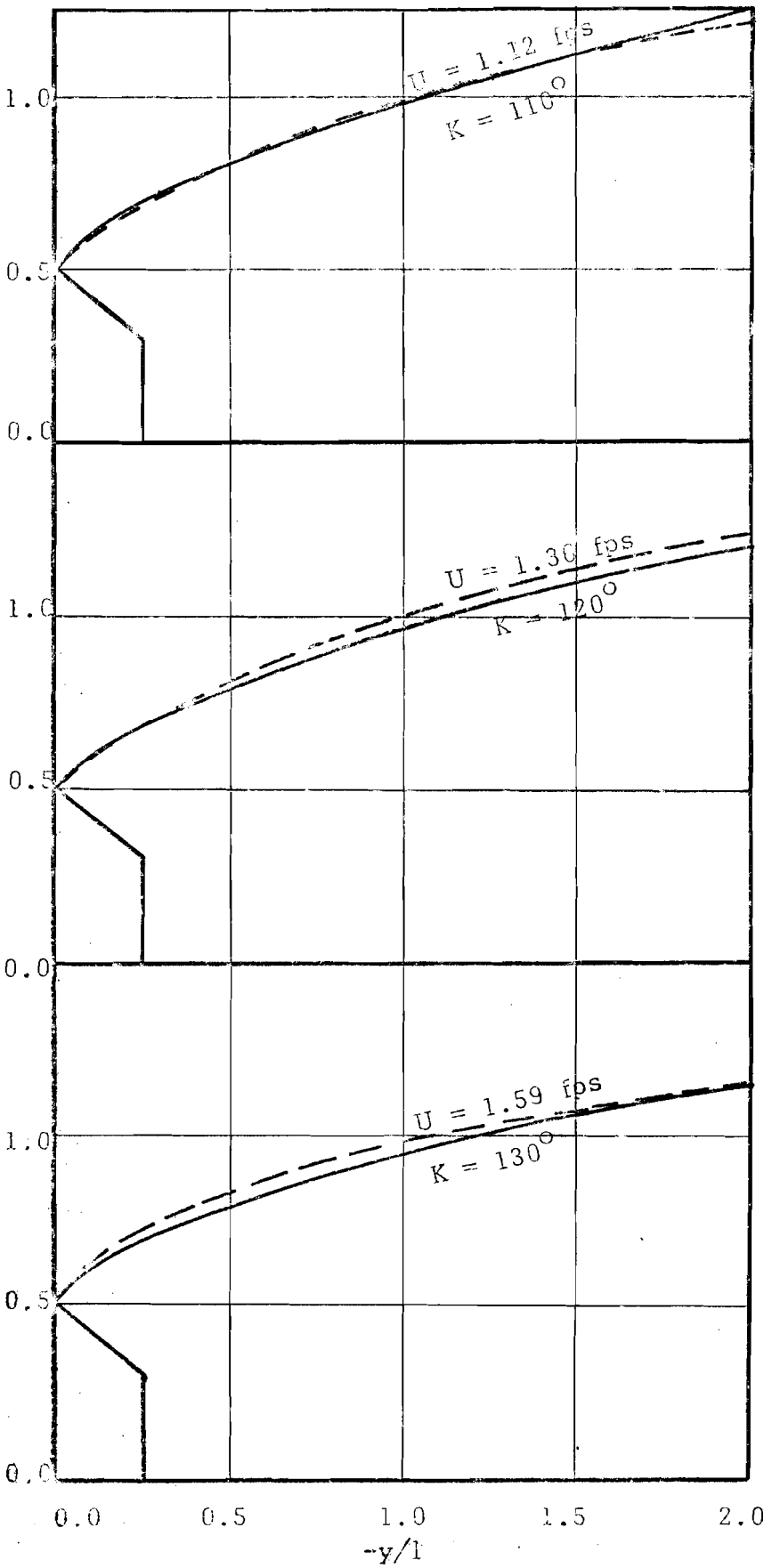

Figure 32. A comparison of wake boundaries (solid line) with observed wake boundaries (dashed line) at h/l = 3.0 and r/h = 0.25.

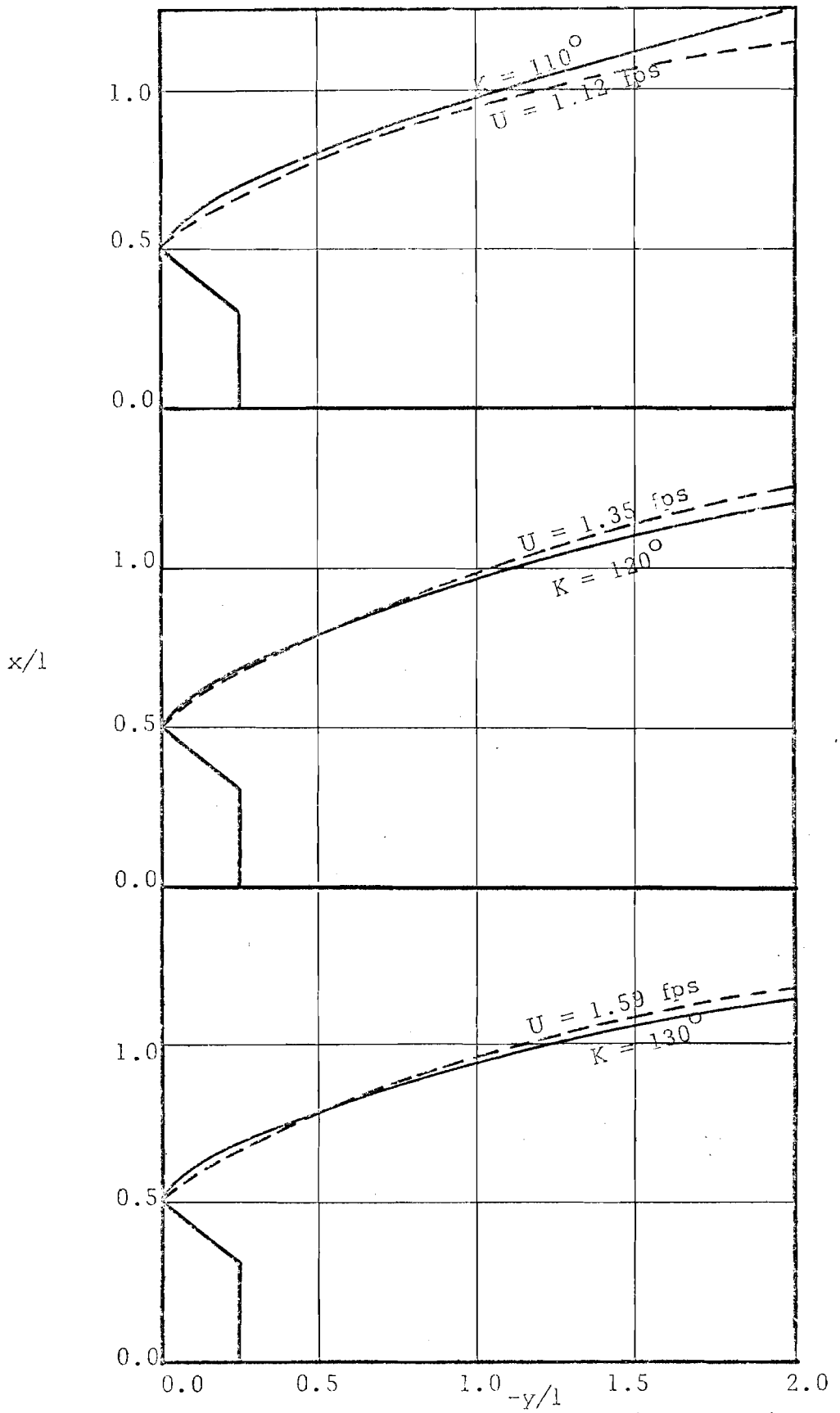

Figure 33. A comparison of wake boundaries (solid line) with observed wake boundaries (dashed line) at h/l = 3.0 and r/h = 0.50.

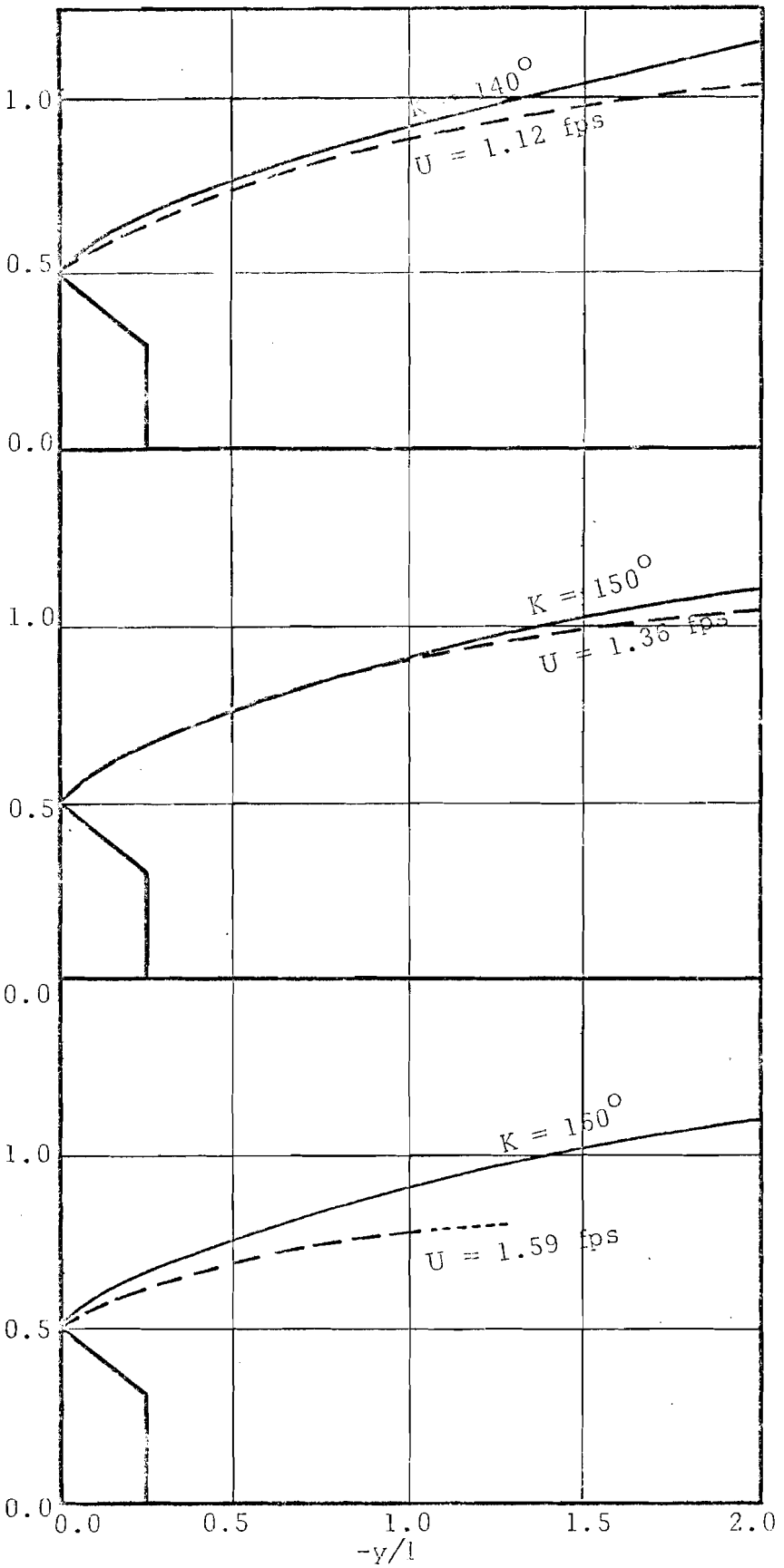

Figure 34. A comparison of wake boundaries (solid line) with observed wake boundaries (dashed line) at h/l = 3.0 and r/h = 0.75.

found in the literature review. Also, gravity forces were completely disregarded during the development of the model. It is assumed that the non-uniformity of K value throughout the water depth is caused by gravity forces, as evidenced by the variation in depth of the water surface. At a high approach velocity, the water surface drops significantly behind the plate and the flow near the water surface is no longer two dimensional. The hollow region behind the plate causes the water to flow inward and downward toward the longitudinal axis. The flow near the water surface is governed by gravity instead of inertia alone. This explains why the theory deviates from the experiment when the shear layer is near the water surface and the approach velocity is high.

Suggestions for Further Study

Some aspects of wake boundaries in a horizontal open channel were not covered in this study. They are listed as follows for further study.

1. The relationship between the parameter K and the approach velocity should be investigated. In this study K increased when the approach velocity increased. A more detailed relationship between these two quantities, used in conjunction with experimental data obtained with a model, could provide a means of obtaining a quick estimate of wake boundaries with a simple velocity measurement.
2. The variation of K with respect to water depth by treating the approach velocity as a parameter should be studied. The effect of water depth can then be

encompassed in predictive equations for the wake boundary. This study will also provide a limit beyond which the proposed model no longer applies.

3. The relationship between K and V* at different approach velocities should be established. From Equations 10 and 12 the following equation results:

$$\text{Cot } K = \frac{v^{*2} - 1}{2v^*} \tag{24}$$

Equation 24 together with experimentally determined values of K will provide a means of estimating the velocity at the separation point. This is very hard to measure experimentally.

4. The model discussed in this study has not been verified in supercritical flow. In supercritical flow, ratio of flow velocity to depth is larger than is the case for subcritical flow. With higher inertia the water is "shooting" when passing the plate. The effect of water surface is expected to be less significant. A study of this kind will yield a set of K values for supercritical flow and will make the predictive model more complete.

5. Further study of the wake size of the embedded sphere is needed. The amount of the volume of the sphere embedded under the channel floor changes the relative geometry of the sphere with respect to the incoming water depth, and accordingly, the wake size.

Further experimental work by changing the embedded volume is suggested.

CHAPTER 7

SUMMARY

A new hodograph was developed for predicting the wake boundary behind a flat plate placed normal to the flow and was verified with experimental results. In this model velocities along the shear layer can vary. The classical Kirchhoff's solution for predicting the wake boundary is a special case of this model.

A comparison of the sizes of wakes produced by a flat plate, a 90-degree wedge, and a circular cylinder were made. The effect of the water surface on wake size was investigated. The shape of wakes produced by an embedded sphere at different degrees of submergence was also studied. All experimental work was done in a horizontal straight open channel.

It was found that:

1. For the wake produced by a flat plate perpendicular to the flow, the wake is narrower when the approach velocity is higher.
2. For a prismatic obstacle perpendicular to the flow water surface effects will force the wake to narrow down near the water surface whereas the flow near the channel floor is not affected and is governed only by inertial force.

3. Among the three prismatic obstacles used, the flat plate, the 90-degree wedge and the circular cylinder, the flat plate is the most effective for producing a large wake. The wake produced by the wedge is similar to that of the plate but a little smaller. The wake produced by a circular cylinder is considerably smaller than the other two.
4. The direction of the velocity at the separation point is more important to the wake size than the contact area between the potential flow and the obstacle.
5. For the embedded sphere studied, the degree of submergence is critical to the wake size. The widest wake occurs when the approach flow depth is slightly less than the height above the flow of the embedded sphere.

NOTATIONS

a,b,c,d,e'	constants
f	analytic function defined for convenience of explanation
F	equation of the free boundary of the flow
h	water depth at the test section
H, H_1, H_2, H_3 and H_6	calibration constants for yaw and pitch probes
K	dimensionless parameter
K', K", $\hat{K}$	constants
l	diameter of obstacle defined as the widest dimension in a projection normal to the flow
n	integer
P	intermediate plane for transformation
P_1, P_2, P_3	pressure at the three tubes of yaw or pitch probe
r	coordinate perpendicular to channel floor
S	equation of the solid boundary of the flow
t	time
T	normalized hodograph plane
u	velocity component in x-direction
U	approach velocity
v	velocity component in y-direction
V	velocity

V_1, V_2	velocity at the outer and inner boundaries of the shear layer
v^*	velocity at the breakdown point of the shear layer
W	the conjugate of the complex velocity, $u - iv$
$\bar{W}$	complex velocity, $u + iv$
$\|W\|$	magnitude of W
x	lateral coordinate in physical plane
y	streamwise coordinate in physical plane
z	complex coordinate, $x + iy$
α	direction of velocity relative to the approaching flow
α'	constant with dimension L/T
β'	constant with dimension $(L/T)^2$, the square of the velocity at the separation point
ζ	intermediate plane for transformation
ω	complex potential
ϕ	velocity potential
ψ	stream function
ν	kinematic viscosity

REFERENCES

1. Batchelor, G.K. 1956 "A Proposal Concerning Laminar Wakes Behind Bluff Bodies at Large Reynolds Number" Journal of Fluid Mechanics Vol. 1, p388.

2. Batchelor, G.K. 1970 An Introduction to Fluid Dynamics, Cambridge at the University Press, pp71-108, 255-263, 343-353, 378-386, 409-423.

3. Dean, W.R. 1944 "On the Shearing Motion of Fluid Past a Projection" Proc. Camb. Phil. Soc. Vol. 40, p19.

4. Fage, M.A. and Johansen, F.C. 1928 "Structure of Vortex Sheets" Phil. Mag., Series 7, p5.

5. Goldstein, S. (ed.) 1938 Modern Developments in Fluid Dynamics, Dover Publications, Inc., pp55-65, 550-557.

6. Prandtl, L. and Tietjens, O.G. 1934 Fundamentals of Hydro and Aeromechanics, Dover Publications, Inc., p178.

7. Prandtl, L. and Tietjens, O.G. 1934 Applied Hydro and Aeromechanics, plates at the end of the book. Dover.

8. Rajaratnam, N. and Muralidhar, D. 1967 "Yaw and Pitch Probes" Technical Report, Department of Civil Engineering University of Alberta, Edmonton, Canada.

9. Rouse, H. 1938 Fluid Mechanics for Hydraulic Engineers, Dover Publications, Inc., p314.

10. Rouse, H. 1946 Elementary Mechanics of Fluids, John Wiley & Sons, Inc., p57.

11. Roshko, A. 1953 "On the Development of Turbulent Wake from Vortex Streets" National Advisory Committee for Aeronautics, Technical Note 2913.

12. Roshko, A. 1954 "A New Hodograph for Free-Streamline Theory", NACA TN 3168.

13. Schlichting, H. 1968 Boundary Layer Theory, McGraw-Hill Book Company, Chapter 7.

14. Shair, F.H., et.al. 1964 "An Experimental Investigation of The Steady Separated Flow Past a Circular Cylinder" Journal of Fluid Mechanics, Vol. 19, p60.

15. Streeter, V.L. 1948 Fluid Dynamics, McGraw-Hill Book Company, Inc. pp177-180.

16. Thom, A. 1933 "The Flow Past Circular Cylinder at Low Speed" Proc. Roy. Soc. A141, p651.

17. Thompson 1960 Theoretical Hydrodynamics, 4th Edition, The MacMillan Company, p315.

18. Townsend, A.A. 1947 "Measurements in the Turbulent Wake of a Cylinder" Proc. Roy. Soc. A 190, p551.

19. Townsend, A.A. 1949 "Momentum and Energy Diffusion in the Turbulent Wake of a Cylinder" Proc. Roy. Soc. A 197, p551.

APPENDIX A

DERIVATIONS OF EQUATIONS 21 AND 23

Derivation of Equation 21:

When $\phi < \frac{\hat{K}}{2}$

$$\left(\frac{\sqrt{\frac{2\phi}{\hat{K}}} - 1}{\sqrt{\frac{2\phi}{\hat{K}}} + 1} \right)^{\frac{\Pi-K}{\Pi}} = [E\ (-1)]^{\frac{\Pi-K}{\Pi}}$$

$$= [E\ e^{i(2n+1)\Pi}]^{\frac{\Pi-K}{\Pi}}$$

If we use the principal branch by setting n equal zero, we have

$$\left(\frac{\sqrt{\frac{2\phi}{\hat{K}}} - 1}{\sqrt{\frac{2\phi}{\hat{K}}} + 1} \right)^{\frac{\Pi-K}{\Pi}} = E^{\frac{\Pi-K}{\Pi}} e^{i(\Pi-K)}$$

Therefore,

$$2\ [1 - \left(\frac{\sqrt{\frac{2\phi}{\hat{K}}} - 1}{\sqrt{\frac{2\phi}{\hat{K}}} + 1} \right)^{\frac{\Pi-K}{\Pi}}\ e^{iK}]^{-1} - 1$$

$$= 2\ [1 - E^{\frac{\Pi-K}{\Pi}} e^{i(\Pi-K)} e^{iK}]^{-1} - 1$$

$$= 2\ [1 - E^{\frac{\Pi-K}{\Pi}} e^{i\Pi}]^{-1} - 1$$

$$= 2\ [1 - E^{\frac{\Pi-K}{\Pi}} (-1)]^{-1} - 1$$

$$= 2\ [1 + E^{\frac{\Pi-K}{\Pi}}]^{-1} - 1$$

$$= \frac{2 - 1 - E^{\frac{\Pi-K}{\Pi}}}{1 + E^{\frac{\Pi-K}{\Pi}}}$$

$$= \frac{1 - E^{\frac{\Pi-K}{\Pi}}}{1 + E^{\frac{\Pi-K}{\Pi}}} ,$$

$$\int \left\{ 2 \left[1 - \left(\frac{\sqrt{\frac{2\phi}{\hat{K}}} - 1}{\sqrt{\frac{2\phi}{\hat{K}}} + 1} \right)^{\frac{\Pi-K}{\Pi}} e^{iK} \right]^{-1} - 1 \right\}^{-1} d\phi$$

$$= \int \frac{1 + E^{\frac{\Pi-K}{\Pi}}}{1 - E^{\frac{\Pi-K}{\Pi}}} \, d\phi$$

Then Equation 21-a follows.

When $\phi > \frac{\hat{K}}{2}$

$$\left\{ 2 \left[1 - E^{\frac{\Pi-K}{\Pi}} e^{iK} \right]^{-1} - 1 \right\}^{-1}$$

$$= \left\{ 2 \left[1 - E^{\frac{\Pi-K}{\Pi}} (\mathrm{Cos}K + i\mathrm{Sin}K) \right]^{-1} - 1 \right\}^{-1}$$

$$= \left\{ \frac{2}{1 - E^{\frac{\Pi-K}{\Pi}} \mathrm{Cos}K - iE^{\frac{\Pi-K}{\Pi}} \mathrm{Sin}K} - 1 \right\}^{-1}$$

$$= \left\{ \frac{1 + E^{\frac{\Pi-K}{\Pi}} \mathrm{Cos}K + iE^{\frac{\Pi-K}{\Pi}} \mathrm{Sin}K}{1 - E^{\frac{\Pi-K}{\Pi}} \mathrm{Cos}K - iE^{\frac{\Pi-K}{\Pi}} \mathrm{Sin}K} \right\}^{-1}$$

$$= \frac{1 - E^{\frac{\Pi-K}{\Pi}} \mathrm{Cos}K - iE^{\frac{\Pi-K}{\Pi}} \mathrm{Sin}K}{1 + E^{\frac{\Pi-K}{\Pi}} \mathrm{Cos}K + iE^{\frac{\Pi-K}{\Pi}} \mathrm{Sin}k}$$

$$= \frac{1 - E^{\frac{2(\Pi - K)}{\Pi}}}{1 + 2E^{\frac{\Pi-K}{\Pi}} \mathrm{Cos}K + E^{\frac{2(\Pi-K)}{\Pi}}} - i \frac{2E\mathrm{Sin}K}{1 + 2E^{\frac{\Pi-K}{\Pi}} \mathrm{Cos}K + E^{\frac{2(\Pi-K)}{\Pi}}}$$

Then Equation 21-b follows.

Derivation of Equation 23.

For $\zeta \neq 0$ and $1 \geq \zeta > -1$

$$\left(\frac{\zeta-1}{\zeta+1}\right)^{\frac{\Pi-K}{\Pi}} = \left(\left|\frac{\zeta-1}{\zeta+1}\right| \quad (-1)\right)^{\frac{\Pi-K}{\Pi}}$$

$$= \left(\left|\frac{\zeta-1}{\zeta+1}\right| e^{i(2n+1)\Pi}\right)^{\frac{\Pi-K}{\Pi}}$$

Similarly, by use of the principal branch by setting n equal zero, we have

$$\left(\frac{\zeta-1}{\zeta+1}\right)^{\frac{\Pi-K}{\Pi}} = \left|\frac{\zeta-1}{\zeta+1}\right|^{\frac{\Pi-K}{\Pi}} e^{i(\Pi-K)}$$

Then,

$$\int\left\{2\left[1 - \left(\frac{\zeta-1}{\zeta+1}\right)^{\frac{\Pi-K}{\Pi}} e^{iK}\right]^{-1} - 1\right\}^{-1} \zeta \, d\zeta$$

$$= \int\left\{2\left[1 - \left|\frac{\zeta-1}{\zeta+1}\right|^{\frac{\Pi-K}{\Pi}} e^{i\Pi}\right]^{-1} - 1\right\}^{-1} \zeta \, d\zeta$$

$$= \int\left\{2\left[1 + \left|\frac{\zeta-1}{\zeta+1}\right|^{\frac{\Pi-K}{\Pi}}\right]^{-1} - 1\right\}^{-1} \zeta \, d\zeta$$

$$= \int\left(\frac{1 + \left|\frac{\zeta-1}{\zeta+1}\right|^{\frac{\Pi-K}{\Pi}}}{1 - \left|\frac{\zeta-1}{\zeta+1}\right|^{\frac{\Pi-K}{\Pi}}}\right) \zeta \, d\zeta$$

For $\zeta > 1$,

$$\left\{2\left[1 - \left(\frac{\zeta-1}{\zeta+1}\right)^{\frac{\Pi-K}{\Pi}} e^{Ki}\right]^{-1} - 1\right\}^{-1}$$

$$= \left\{2\left[1 - \left(\frac{\zeta-1}{\zeta+1}\right)^{\frac{\Pi-K}{\Pi}} (\mathrm{Cos}K + i\mathrm{Sin}K)\right]^{-1} - 1\right\}^{-1}$$

$$= \left\{\frac{2 - \left[1 - \left(\frac{\zeta-1}{\zeta+1}\right)^{\frac{\Pi-K}{\Pi}} \mathrm{Cos}K - i\left(\frac{\zeta-1}{\zeta+1}\right)^{\frac{\Pi-K}{\Pi}} \mathrm{Sin}K\right]}{1 - \left(\frac{\zeta-1}{\zeta+1}\right)^{\frac{\Pi-K}{\Pi}} \mathrm{Cos}K - i\left(\frac{\zeta-1}{\zeta+1}\right)^{\frac{\Pi-K}{\Pi}} \mathrm{Sin}K}\right\}^{-1}$$

$$= \left(\frac{1 + \left(\frac{\zeta-1}{\zeta+1}\right)^{\frac{\Pi-K}{\Pi}} \mathrm{Cos}K + i\left(\frac{\zeta-1}{\zeta+1}\right)^{\frac{\Pi-K}{\Pi}} \mathrm{Sin}K}{1 - \left(\frac{\zeta-1}{\zeta+1}\right)^{\frac{\Pi-K}{\Pi}} \mathrm{Cos}K - i\left(\frac{\zeta-1}{\zeta+1}\right)^{\frac{\Pi-K}{\Pi}} \mathrm{Sin}K}\right)^{-1}$$

$$= \frac{1 - \left(\frac{\zeta-1}{\zeta+1}\right)^{\frac{\Pi-K}{\Pi}} \mathrm{Cos}K - i\left(\frac{\zeta-1}{\zeta+1}\right)^{\frac{\Pi-K}{\Pi}} \mathrm{Sin}K}{1 + \left(\frac{\zeta-1}{\zeta+1}\right)^{\frac{\Pi-K}{\Pi}} \mathrm{Cos}K + i\left(\frac{\zeta-1}{\zeta+1}\right)^{\frac{\Pi-K}{\Pi}} \mathrm{Sin}K}$$

$$= \frac{\left(1 - \left(\frac{\zeta-1}{\zeta+1}\right)^{\frac{\Pi-K}{\Pi}} \mathrm{Cos}K\right)\left(1 + \left(\frac{\zeta-1}{\zeta+1}\right)^{\frac{\Pi-K}{\Pi}} \mathrm{Cos}K\right) - \left[\left(\frac{\zeta-1}{\zeta+1}\right)^{\frac{\Pi-K}{\Pi}} \mathrm{Sin}K\right]^2}{\left[1 + \left(\frac{\zeta-1}{\zeta+1}\right)^{\frac{\Pi-K}{\Pi}} \mathrm{Cos}K\right]^2 + \left[\left(\frac{\zeta-1}{\zeta+1}\right)^{\frac{\Pi-K}{\Pi}} \mathrm{Sin}K\right]^2}$$

$$-i\,\frac{\left(\frac{\zeta-1}{\zeta+1}\right)^{\frac{\Pi-K}{\Pi}} (\mathrm{Sin}K)\left(1 + \left(\frac{\zeta-1}{\zeta+1}\right)^{\frac{\Pi-K}{\Pi}} \mathrm{Cos}K\right) + \left(\frac{\zeta-1}{\zeta+1}\right)^{\frac{\Pi-K}{\Pi}} (\mathrm{Sin}K)\left(1 - \left(\frac{\zeta-1}{\zeta+1}\right)^{\frac{\Pi-K}{\Pi}} \mathrm{Cos}K\right)}{\left[1 + \left(\frac{\zeta-1}{\zeta+1}\right)^{\frac{\Pi-K}{\Pi}} \mathrm{Cos}K\right]^2 + \left[\left(\frac{\zeta-1}{\zeta+1}\right)^{\frac{\Pi-K}{\Pi}} \mathrm{Sin}K\right]^2}$$

$$= \frac{1 - \left(\frac{\zeta-1}{\zeta+1}\right)^{\frac{2(\Pi-K)}{\Pi}}}{1 + 2\left(\frac{\zeta-1}{\zeta+1}\right)^{\frac{\Pi-K}{\Pi}} \mathrm{Cos}K + \left(\frac{\zeta-1}{\zeta+1}\right)^{\frac{2(\Pi-K)}{\Pi}}}$$

$$-i \frac{2\left(\frac{\zeta-1}{\zeta+1}\right)^{\frac{\Pi-K}{\Pi}} \mathrm{Sin}K}{1 + 2\left(\frac{\zeta-1}{\zeta+1}\right)^{\frac{\Pi-K}{\Pi}} \mathrm{Cos}K + \left(\frac{\zeta-1}{\zeta+1}\right)^{\frac{2(\Pi-K)}{\Pi}}}$$

Together with Equations A-1 and A-2, Equation 23 follows.

APPENDIX B

COMPUTER PROGRAM FOR THE NUMERICAL INTEGRATION OF EQUATION 23

NUMERICAL INTEGRATION FOR EQUATION 23

```
      DR(X)=X*(1.+ABS((X-1.)/(X+1.))**((3.14159-XK)/3.14159))/(1.-ABS((X
     1-1.)/(X+1.))**((3.14159-XK)/3.14159))
      F(X)=X*(1.-((X-1.)/(X+1.))**(2.*(3.14159-XK)/3.14159))/(1.+2.*COS(
     1XK)*((X-1.)/(X+1.))**((3.14159-XK)/3.14159)+((X-1.)/(X+1.))**(2.*(
     2(3.14159-XK)/3.14159)))
      FUNB(X)=2.*X*((X-1.)/(X+1.))**((3.14159-XK)/3.14159)*SIN(XK)/(1.+2
     1.*COS(XK)*((X-1.)/(X+1.))**((3.14159-XK)/3.14159)+((X-1.)/(X+1.))*
     2*(2.*((3.14159-XK)/3.14159))
    1 FORMAT(1H1,'INTEGRAL VALUES FOR DIFFERENT UPPER INTEGRATION LIMITS
     1'///)
    2 FORMAT(3X,28HTRAPEZOIDAL RULE, INTEGRAL A./10X,49H          A
     1          X              INTEGRAL VALUE/)
    3 FORMAT(18X,F10.7,6X,F10.7,6X,F15.7)
    4 FORMAT(/3X,28HTRAPEZOIDAL RULE, INTEGRAL B./10X,49H          A
     1          X              INTEGRAL VALUE/)
    7 FORMAT(5(2XF10.7))
    8 FORMAT(1H ,5X,F12.7)
   22 FORMAT(1H1,16(2(5X,F15.7)/))
      DIMENSION ATA(2000),ATB(2000),ART(200),AIT(200),T(400)
      XKINC=3.14159/18.
      J=1
      READ(1,7)A,B,XK,C,D
   33 WRITE(3,1)
      XKDG=180.*XK/3.14159
      WRITE(3,8)XKDG
      WRITE(3,2)
      N=1024
      H=(B-A)/FLOAT(N)
      SUMTA=DR(A)
      X=A
      DO 10 K=1,N
      X=X+H
      IF((X.LT.1.E-6).AND.(X.GT.-1.E-6)) GO TO 131
      SUMTA+SUMTA+2.*DR(X)
      IF(64*(K/64).NE.K) GO TO 10
      SUMTAP-(SUMTA-DR(X))*H/2.
      GO TO 121
  131 Z=-3.14159/(3.14159-XK)
      SUMTA=SUMTA+2.*Z
      IF(64*(K/64).NE.K) GO TO 10
      SUMTAP=(SUMTA-Z)*H/2.
  121 WRITE(3,3) A,X,SUMTAP
   10 CONTINUE
      DOWN=SUMTAP
```

```
      WRITE(3,1)
      WRITE(3,2)
      H=(D-C)/FLOAT(N)
      SUMTA=F(C)
      X=C
      DO 100 K=1,N
      X=X+H
      SUMTA=SUMTA+2.*F(X)
      IF(64*(K/64).NE.K) GO TO 100
      SUMTAP=(SUMTA-F(X))*H/2.
      WRITE(3,3)C,X,SUMTAP
      ATA(K)=SUMTAP
  100 CONTINUE
      WRITE(3,4)
      Y=C
      SUMTB=FUNB(Y)
      DO 300  K=1,N
      Y=Y+H
      SUMTB=SUMTB+2.*FUNB(Y)
      IF(64*(K/64).NE.K) GO TO 300
      SUMTBP=(SUMTB-FUNB(Y))*H/2.
      WRITE(3,3)C,Y,SUMTBP
      ATB(K)=SUMTBP
  300 CONTINUE
      DO 11 I=1,16
      M=I*64
      ART(I)=ATA(M)/DOWN+0.5
      AIT(I)=ATB(M)/DOWN
      T(I)=ART(I)
      L=I+16
      T(L)=AIT(K)
   11 CONTINUE
      WRITE(3,22) (ART(I),AIT(I),I=1,16)
      CALL PLOT (1,T,16,2,0,0)
      XK=XK+XKINC
      J=J+1
      IF(J.GT.9) GO TO 44
      GO TO 33
   44 STOP
      END
```

APPENDIX C

COMPUTER PROGRAM FOR VELOCITY CALCULATIONS

VELOCITY CALCULATIONS

```
      DOUBLE PRECISION XK,XK6,DELTAH,RANGLE,ALPHA,VK6,ANGLE(200),VELOTY(
     1200),U(200),V(200),XK1(200),XK3(200),VSCALD(200),US(200),VS(200),H
      ALPHA(X)=0.2132639229DO2+X*(-0.4139719246DO2+X*(0.6696645438DO1+X*
     1(0.5554788458DO2+X*(0.1724308016DOO+X*(-0.8587591812DO2+X*(-0.3495
     2613992DO2+X*(0.4263700277DO2+X*(0.3117316260DO2+X*(0.4804188407DO1
     3+X*(-0.1348433474DOO)))))))))
      VK6(X)=0.135110788DO1+X*(-0.5484753459D-01+X*(0.3920271747D-02+X*
     1(-0.1857574152D-03+X*(0.5208180521D-05+X*(-0.7490593001D-07+X*(0.4
     2355005161D-09))))))
      K=1
    5 READ(1,9 N,H
      READ(1,10) (XK1(I),I=1,N),(XK3(I),I=1,N)
      WRITE(3,20)
      WRITE(3,30) (I,XK1(I),XK3(I),I=1,N)
      WRITE(3,40)
      DO 1 I=1,N
      XK=(XK3(I)*1.16.)/(XK1(I)*0.8/17.3)
      DELTAH=DABS(XK1(I))*0.8/(17.3*12.)
      IF(XK.LE.1.) GO TO 2
      XK=1./XK
      ANGLE(I)=-1.*ALPHA(XK)
      GO TO 3
    2 ANGLE(I)=ALPHA(XK)
    3 XK6=VK6(DABS(ANGLE(I)))
      VELOTY(I)=XK6*DSQRT(2.*32.2*DELTAH)
      RANGLE=ANGLE(I)*3.14159/180.
      U(I) =VELOTY(I)*DCOS(RANGLE)
      V(I)=VELOTY(I)*DSIN(RANGLE)
    1 WRITE(3,50) I,VELOTY(I),ANGLE(I),U(I),V(I)
      WRITE(3,60)
      DO 4 I=1,N
      VSCALD(I)=VELOTY(I)/DSQRT(32.2*H)
      US(I)=U(I)/DSQRT(32.2*H)
      VS(I)=V(I)/DSQRT(32.2*H)
    4 WRITE(3,70) I,VSCALD(I),US(I),VS(I)
      K=K+1
      IF(K.LE.6) GO TO 5
    9 FORMAT(I5,F5.3)
   10 FORMAT(16F5.1)
   20 FORMAT(1H1,'CWAKE SP DATA.'//7X,'H1-H2      H3-H2')
   30 FORMAT(1H ,I3,3X,F5.1,7X, F5.1)
```

```
40 FORMAT(1H1,6X,'VELOCITY,FPS    DIRECTION,DEGREE   U,FPS   V,FPS'/)
50 FORMAT(1H ,I3,2X,F7.3,8X,F7.3,12X,F6.3,3X,F6.3)
60 FORMAT(1H1,'VELOCITY/SQRT(GRAVITY*DEPTH)'/6X,'VELOCITY',4X,'U",10X
  1,'V'/)
70 FORMAT(1H ,I3,2X,F7.3,6X,F6.3,6X,F6.3)
   STOP
   END
```

Table C-1. Residuals for the polynomial relating α and H_6

Observation No.	X Value	Y Value	Y Estimate	Total
1	0.0	1,35000	1,35111	-0.00111
2	5.00000	1.16000	1.15468	0.00532
3	10.00000	1.04500	1.05393	-0.00893
4	15.00000	1.00000	0.99527	0.00473
5	20.00000	0.96000	0.95769	0.00231
6	25.00000	0.93500	0.93690	-0.00190
7	30.00000	0.93200	0.93437	-0.00237
8	35.00000	0.95500	0.95132	0.00368
9	40.00000	0.98500	0.98755	-0.00255
10	45.00000	1.04500	1.04521	-0.00022
11	50.00000	1.14000	1.13745	0.00255
12	55.00000	1.30000	1.30198	-0.00198
13	60.00000	1.62000	1.61952	0.00048

Table C-2. Residuals for the polynomial relating H and α.

Observation No.	X Value	Y Value	Y Estimate	Total
1	1.00000	0.0	-0.00638	0.00638
2	0.57300	5.00000	4.99015	0.00985
3	0.33000	10.00000	10.03439	-0.03439
4	0.16700	15.00000	14.84692	0.15308
5	0.02750	20.00000	20.19412	-0.19412
6	-0.08800	25.00000	24.98369	0.01631
7	-0.20900	30.00000	29.79475	0.20525
8	-0.36800	35.00000	35.16594	-0.16594
9	-0.55400	40.00000	39.92758	0.07242
10	-0.80200	45.00000	45.00455	-0.00455
11	-1.15600	50.00000	49.99278	0.00722
12	-1.81200	55.00000	54.99365	0.00635
13	-3.29000	60.00000	60.07010	-0.07010

APPENDIX D

DATA POINTS AND SMOOTHED WAKE BOUNDARIES FOR EACH OBSTACLE

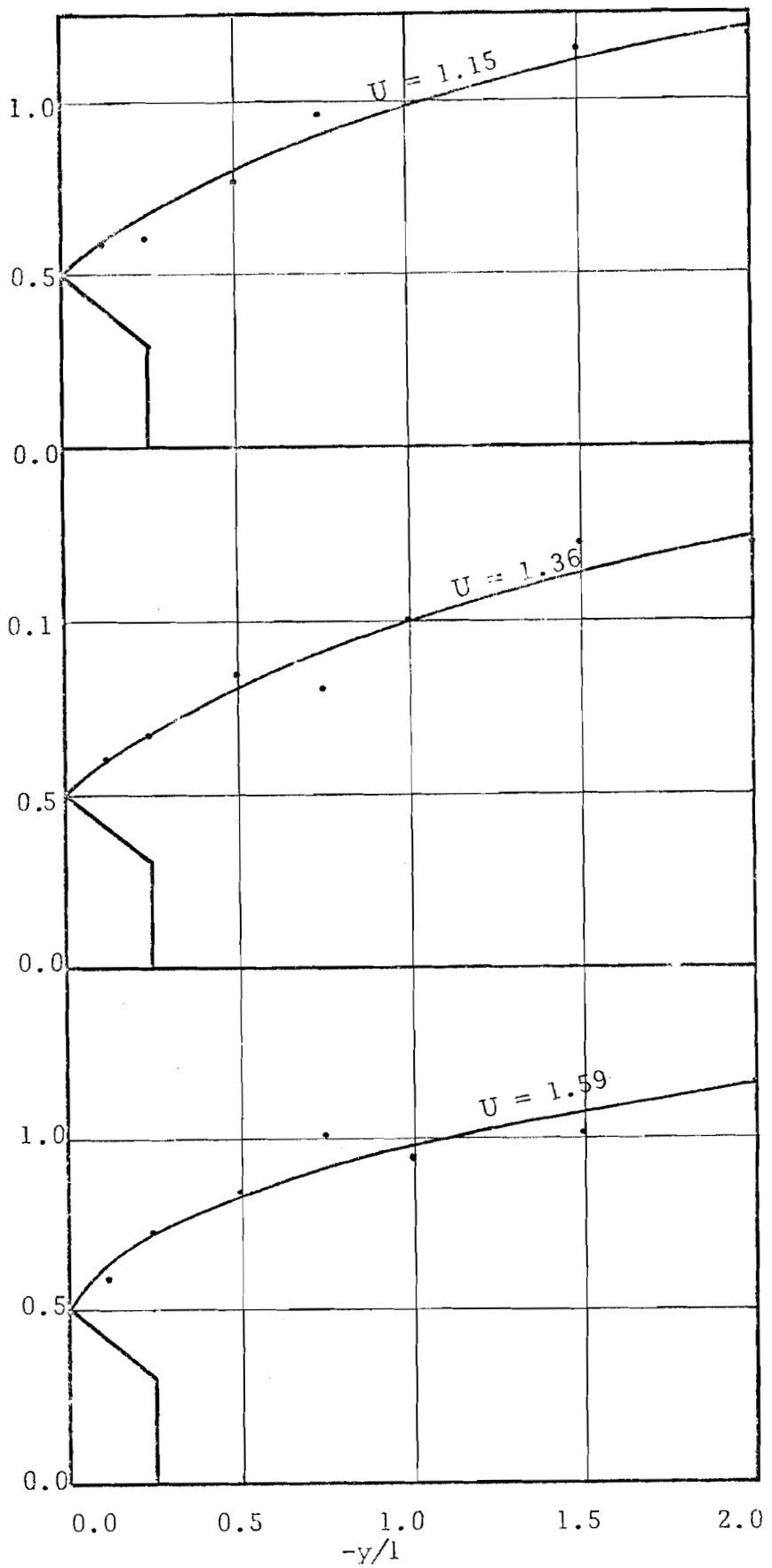

Figure A-1. Data points and smoothed wake boundaries for h/l = 3.0 and r/h = 0.25.

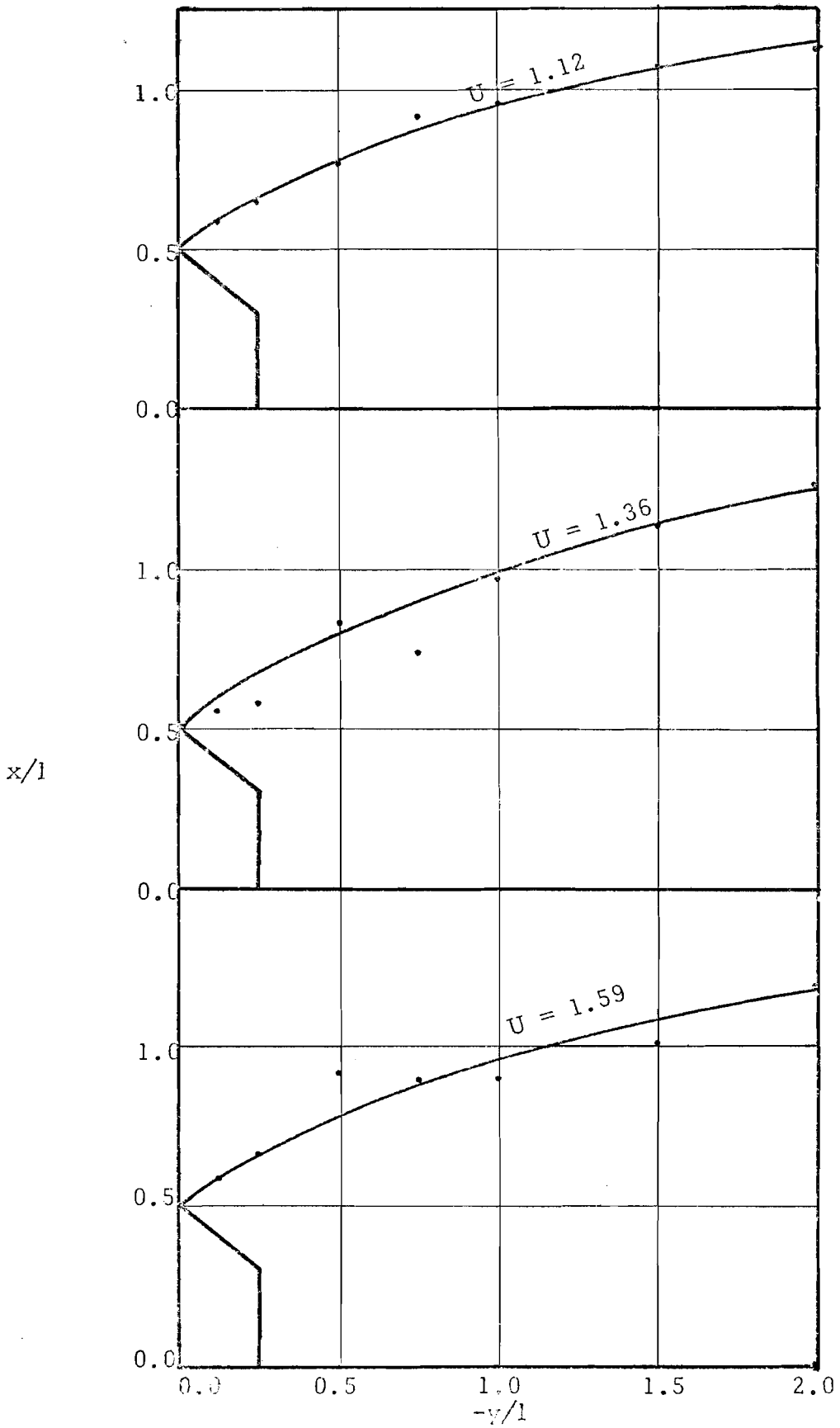

Figure A-2. Data points and smoothed wake boundaries for h/l = 3.0 and r/h = 0.50.

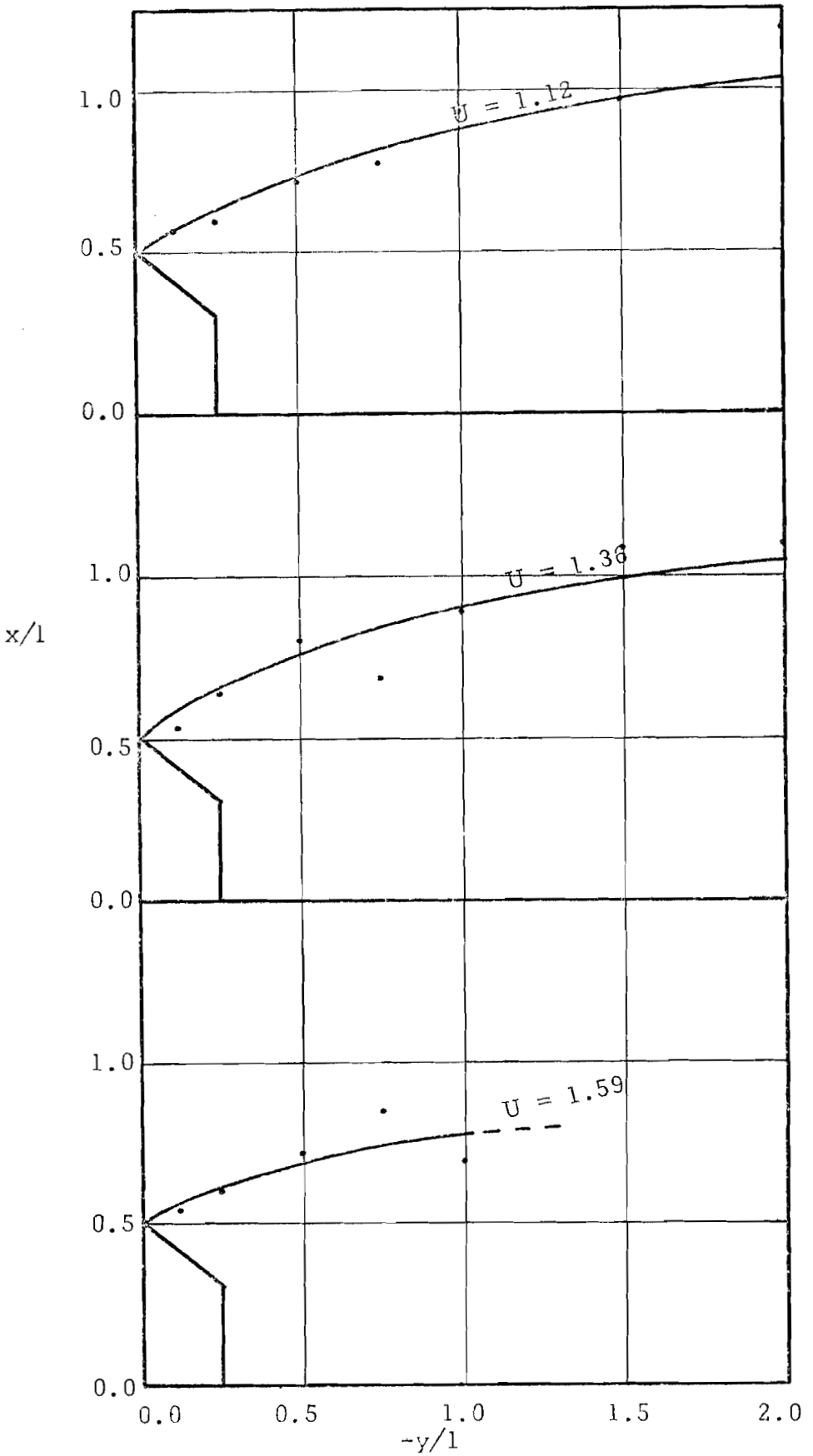

Figure A-3. Data points and smoothed wake boundaries for h/l = 3.0 and r/h = 0.75.

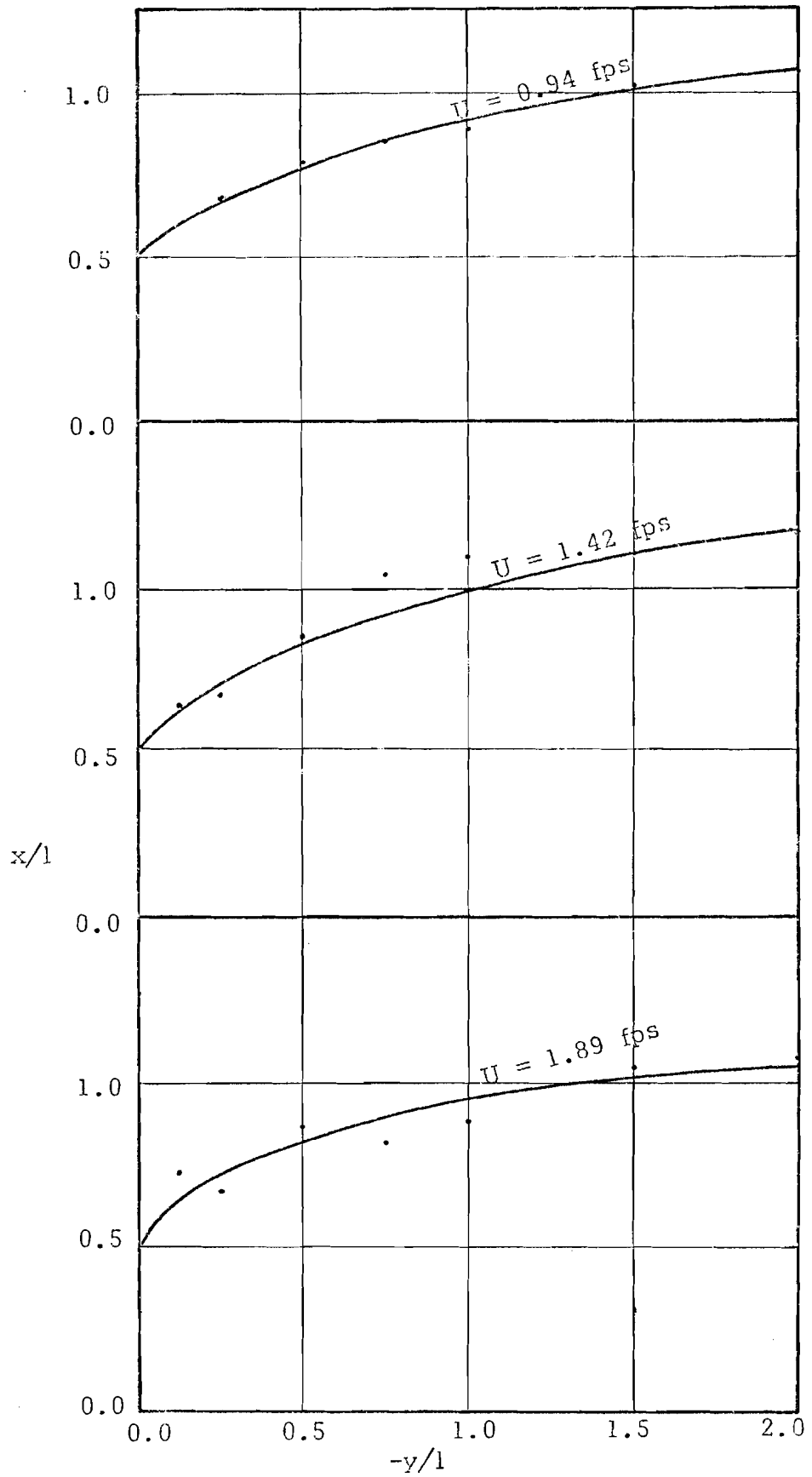

Figure A-4. Data points and smoothed boundary for wake produced by 90° wedge h/l = 3.0, r/h = 0.25.

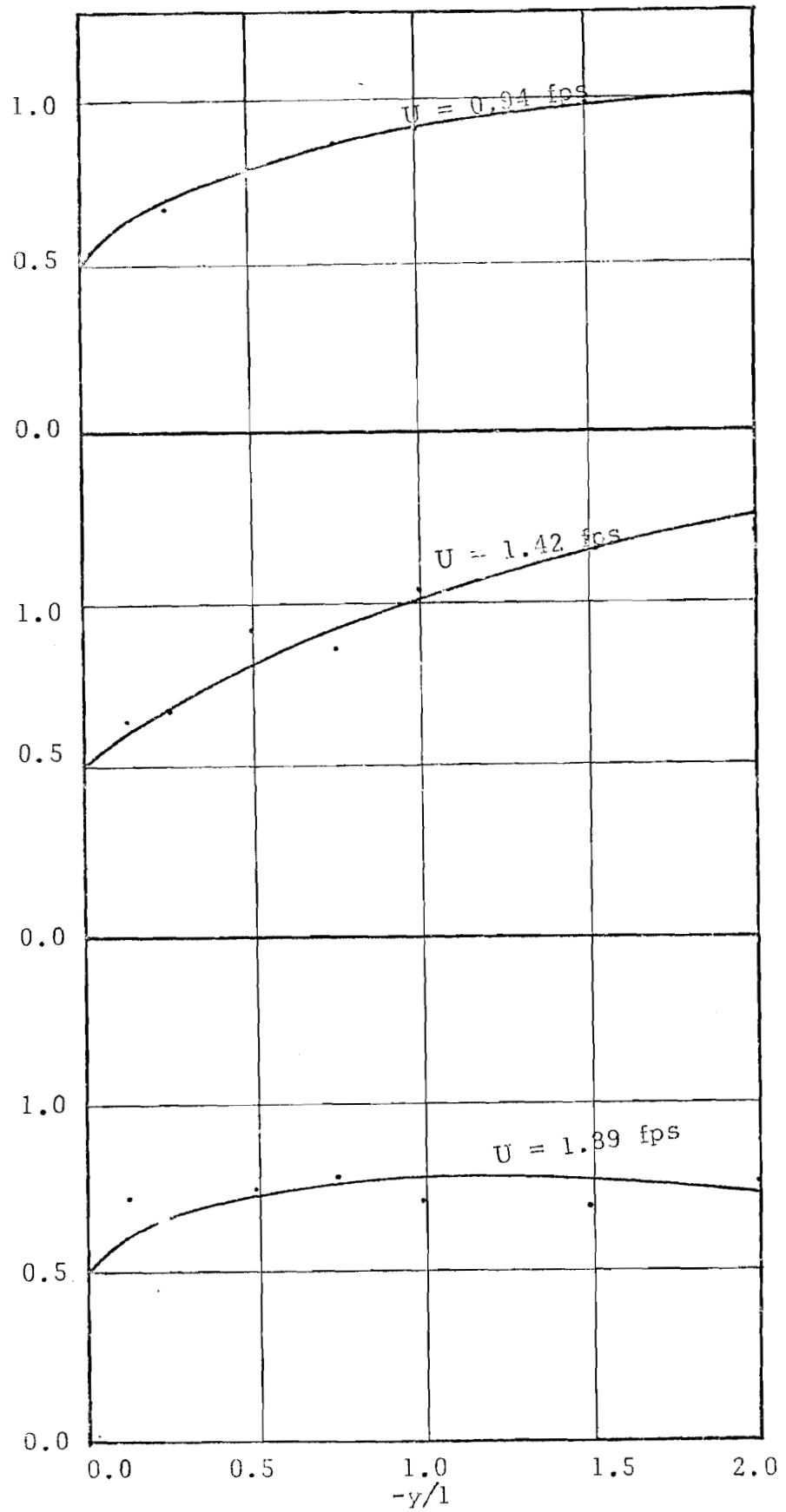

Figure A-5. Data points and smoothed boundary for wake produced by 90° wedge, h/l = 3.0, r/h = 0.50.

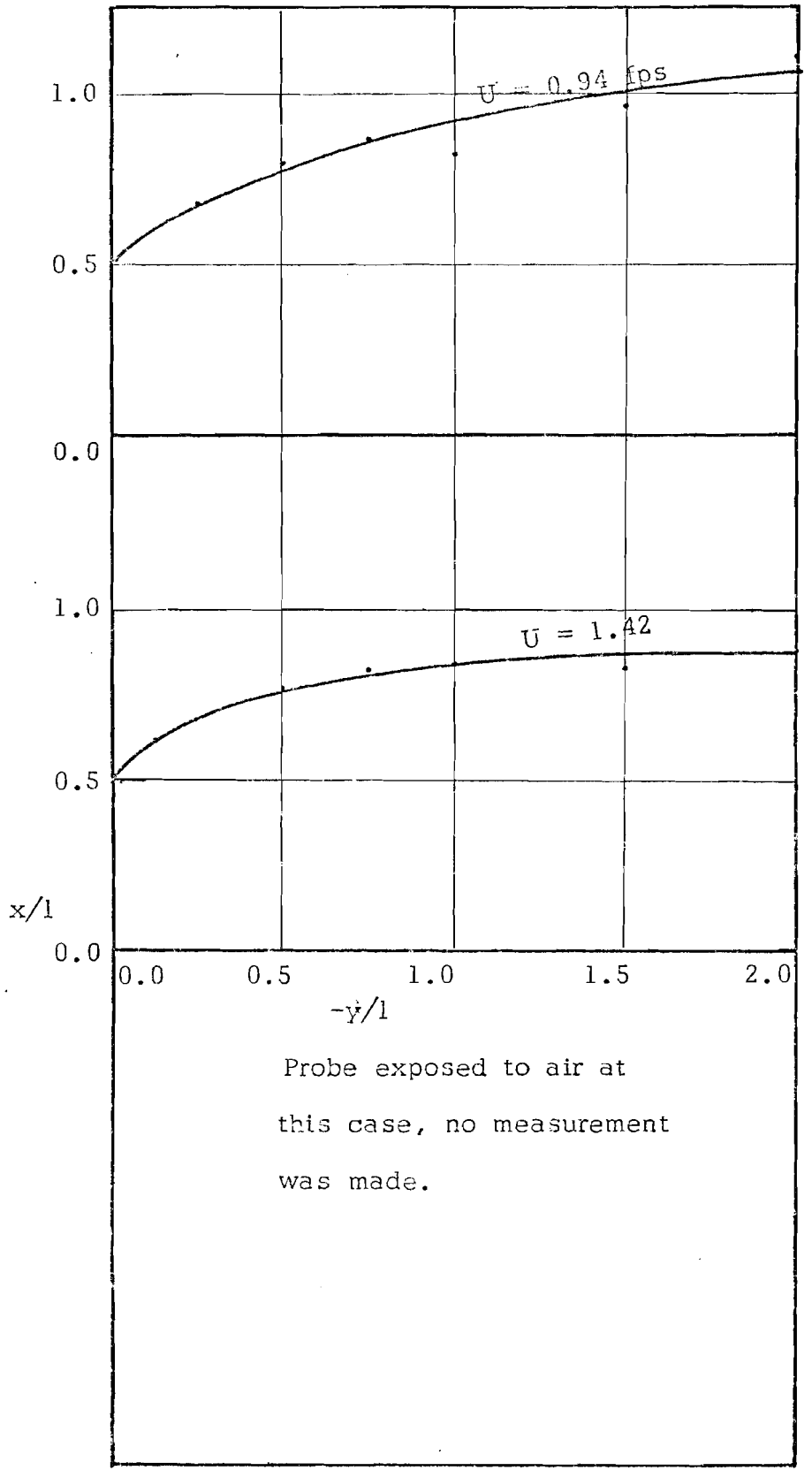

Figure A-6. Data points and smoothed boundary for wake produced by 90° wedge, h/l = 3.0, r/h = 0.75.

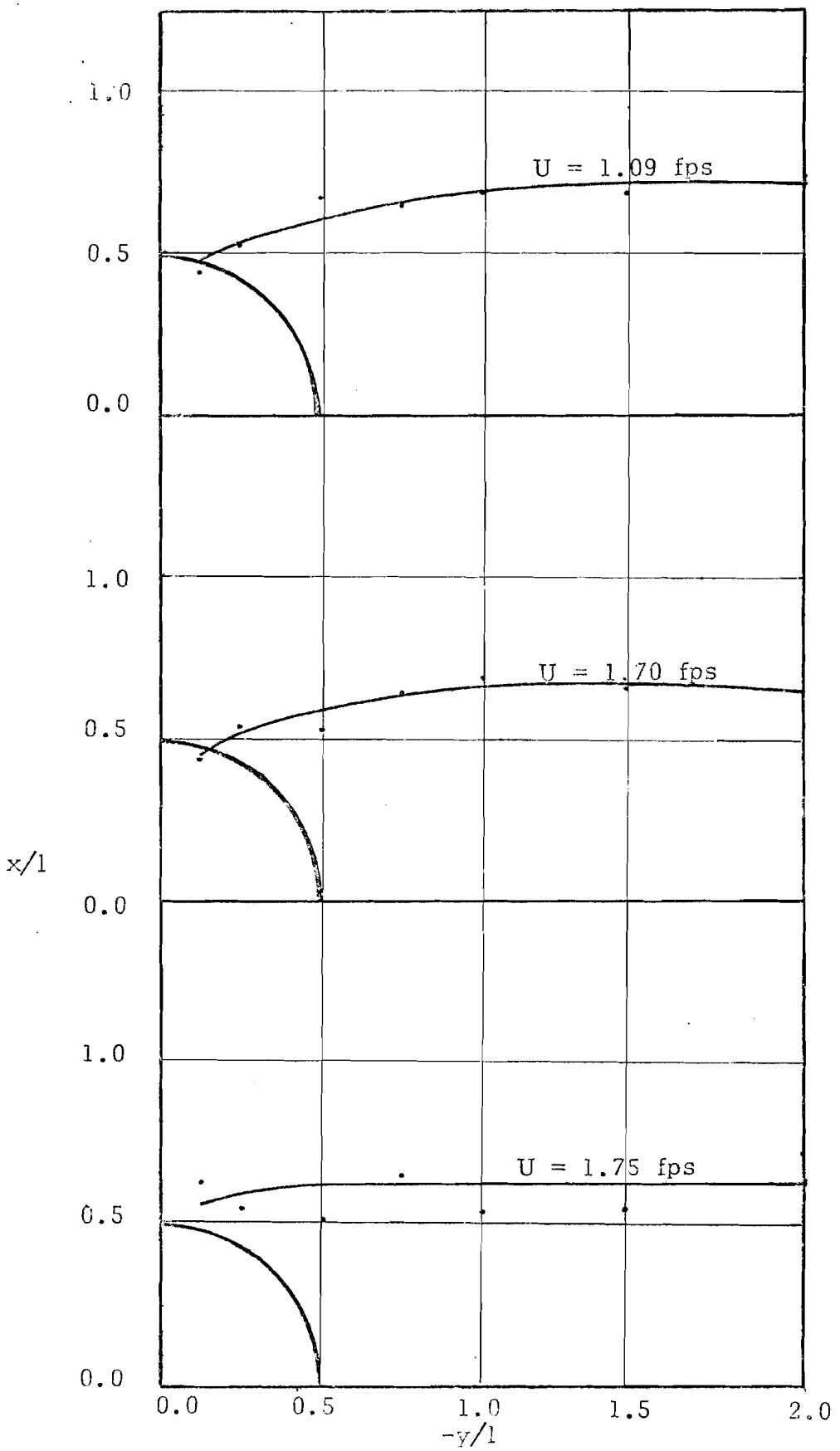

Figure A-7. Data points and smoothed boundaries for wakes produced by a circular cylinder, h/l = 3.0, r/h = 0.25.

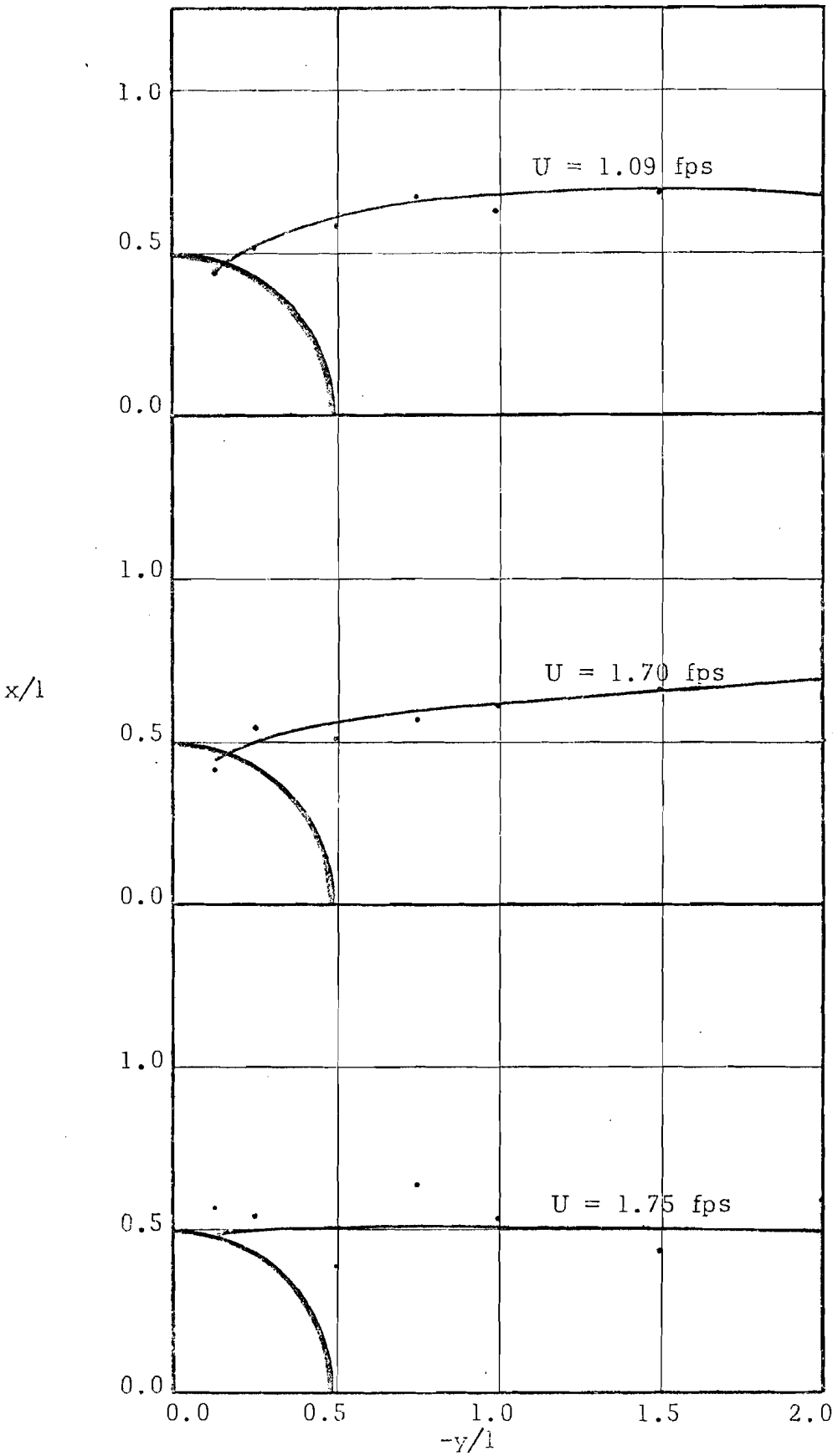

Figure A-8. Data points and smoothed boundaries for wakes produced by a circular cylinder, h/l = 3.0, r/h = 0.50.

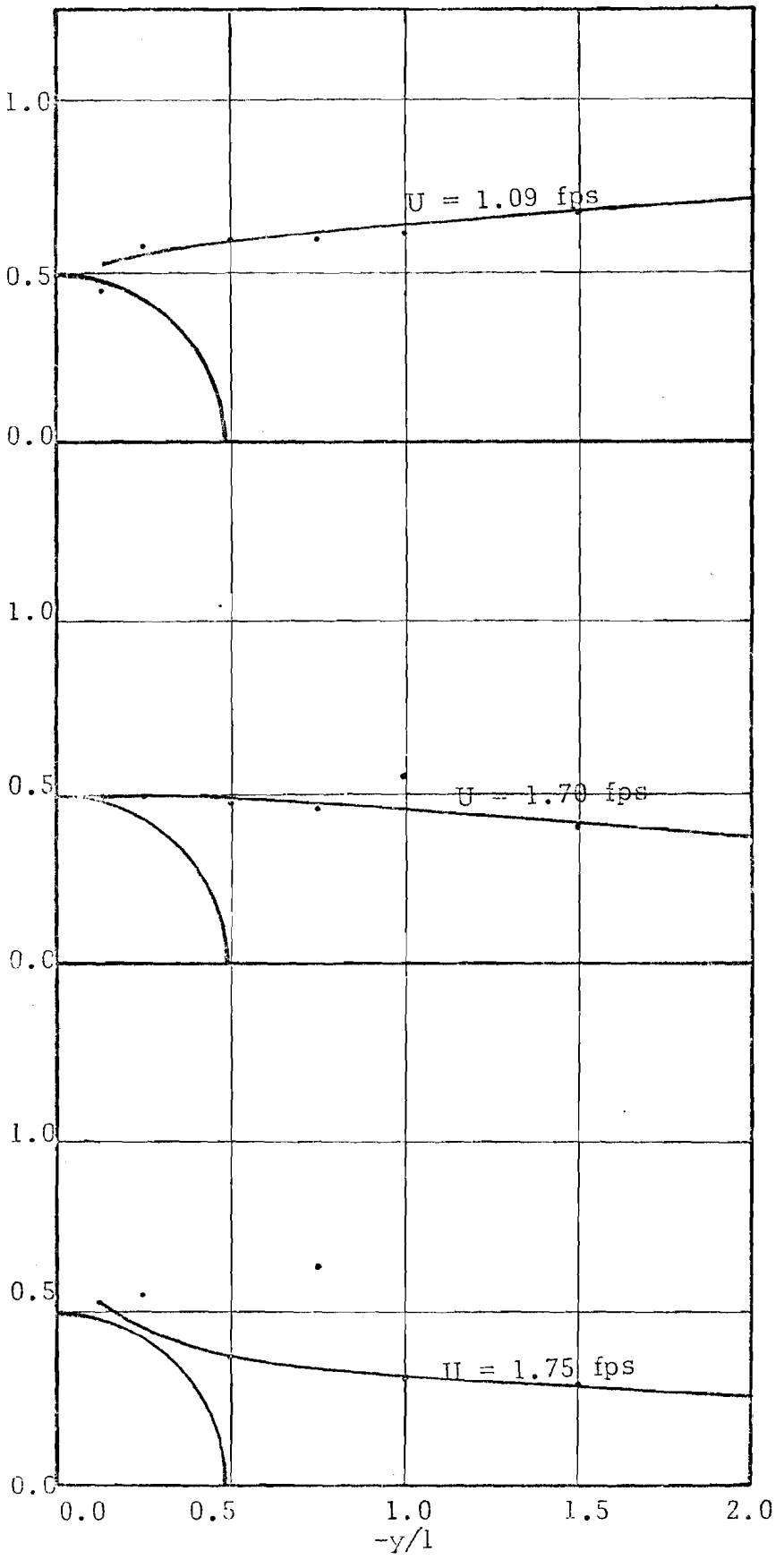

Figure A-9. Data points and smoothed boundaries for wakes produced by a circular cylinder, h/l = 3.0, r/h = 0.75.

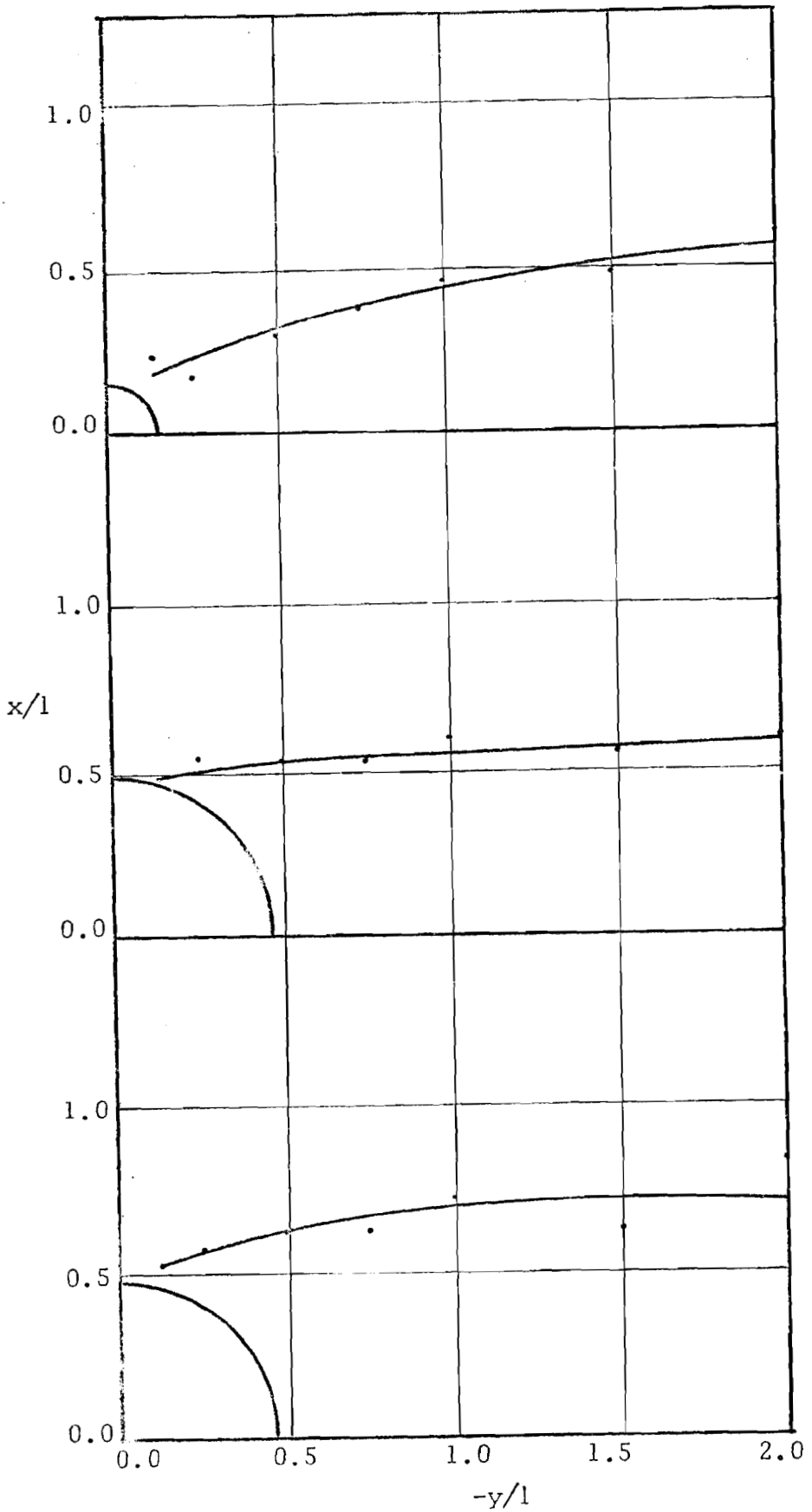

Figure A-10. Data points and smoothed boundaries of wake produced by embedded sphere h/l = 1.0, U = 1.12.

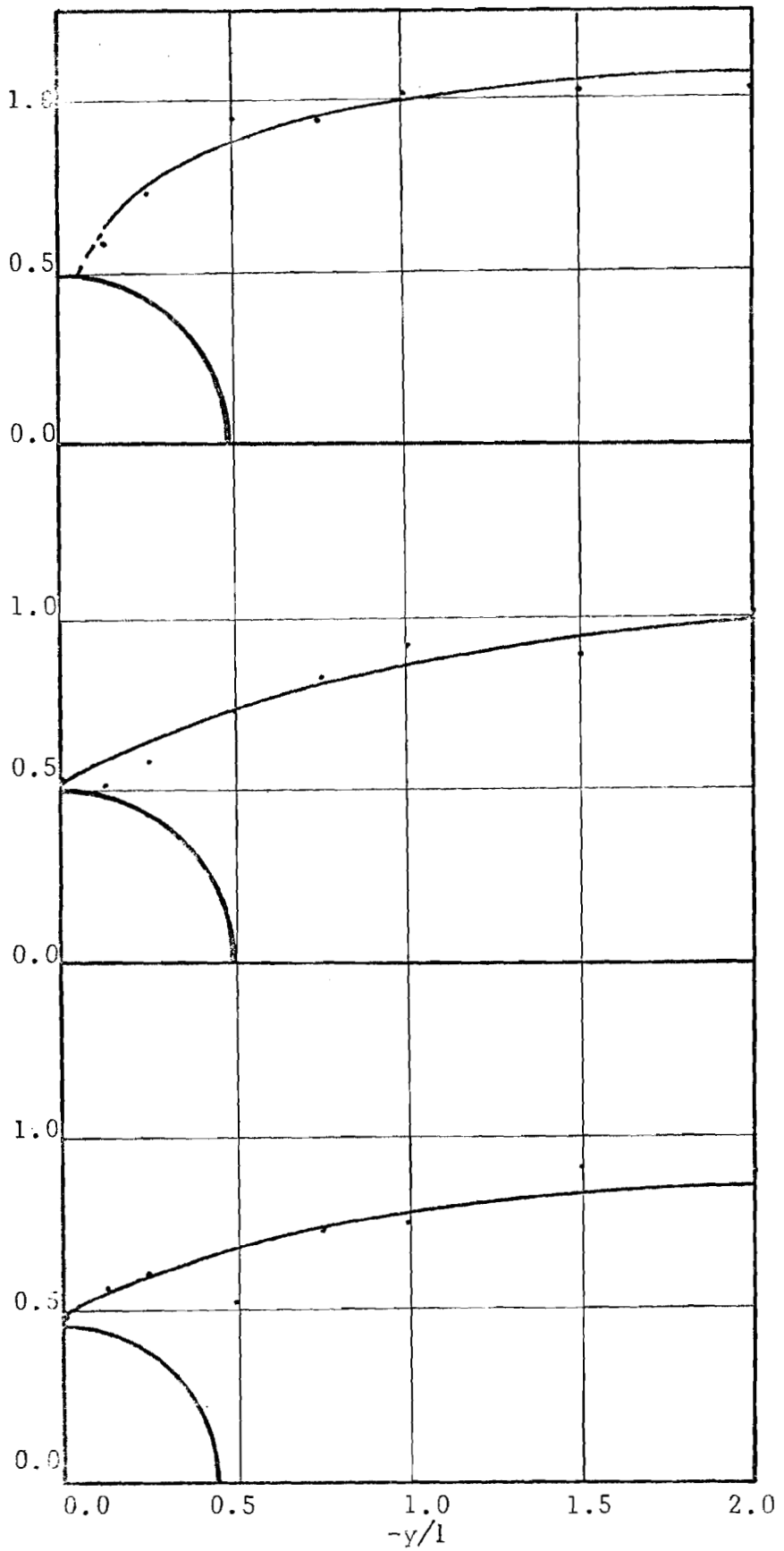

Figure A-11. Data points and smoothed boundaries of wake produced by embedded sphere, h/l = 0.7, U = 1.05.

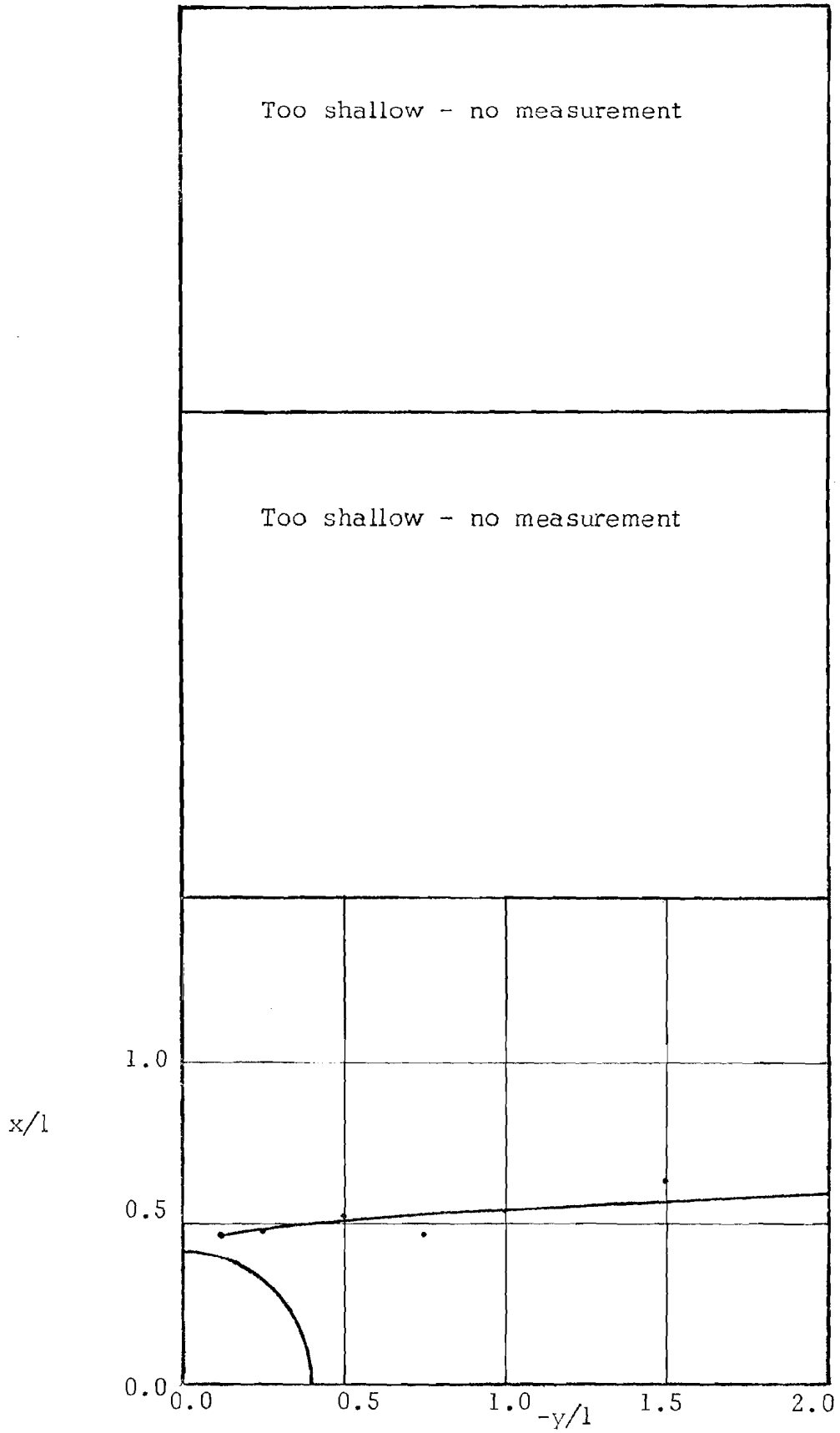

Figure A-12. Data points and smoothed boundaries of wake produced by embedded sphere, h/l = 0.5, U = 1.04.